

AN ANALYSIS OF ALMA DEEP FIELDS AND THE PERCEIVED DEARTH OF HIGH- z GALAXIESCAITLIN M. CASEY,¹ JACQUELINE HODGE,² JORGE A. ZAVALA,¹ JUSTIN SPILKER,¹ ELISABETE DA CUNHA,³
JOHANNES STAGUHN,^{4,5} STEVEN L. FINKELSTEIN,¹ AND PATRICK DREW¹¹*Department of Astronomy, The University of Texas at Austin, 2515 Speedway Blvd Stop C1400, Austin, TX 78712*²*Leiden Observatory, Niels Bohrweg 2, 2333 CA Leiden, The Netherlands*³*Research School of Astronomy and Astrophysics, The Australian National University, Canberra ACT 2611, Australia*⁴*NASA Goddard Space Flight Center, Code 665, Greenbelt, MD 20771*⁵*Bloomberg Center for Physics and Astronomy, Johns Hopkins University 3400 N. Charles Street, Baltimore, MD 21218*

ABSTRACT

Deep, pencil-beam surveys from ALMA at 1.1–1.3 mm have uncovered an apparent absence of high-redshift dusty galaxies, with existing redshift distributions peaking around $z \sim 1.5 - 2.5$. This has led to a perceived dearth of dusty systems at $z \gtrsim 4$, and the conclusion, according to some models, that the early Universe was relatively dust-poor. In this paper, we extend the backward evolution galaxy model described by Casey et. al. (2018) to the ALMA regime (in depth and area) and determine that the measured number counts and redshift distributions from ALMA deep field surveys are fully consistent with constraints of the infrared luminosity function (IRLF) at $z < 2.5$ determined by single-dish submillimeter and millimeter surveys conducted on much larger angular scales ($\sim 1-10 \text{ deg}^2$). We find that measured 1.1–1.3 mm number counts are most constraining for the measurement of the faint-end slope of the IRLF at $z \lesssim 2.5$ instead of the prevalence of dusty galaxies at $z \gtrsim 4$. Recent studies have suggested that UV-selected galaxies at $z > 4$ may be particularly dust-poor, but we find their millimeter-wave emission cannot rule out consistency with the Calzetti dust attenuation law, even by assuming relatively typical, cold-dust ($T_{\text{dust}} \approx 30 \text{ K}$) SEDs. Our models suggest that the design of ALMA deep fields requires substantial revision to constrain the prevalence of $z > 4$ early Universe obscured starbursts. The most promising avenue for detection and characterization of such early dusty galaxies will come from future ALMA 2 mm blank field surveys covering a few hundred arcmin² and the combination of existing and future dual-purpose 3 mm datasets.

Keywords: galaxies: starburst – ISM: dust – cosmology: dark ages – surveys

1. INTRODUCTION

Since its commissioning in 2011, the Atacama Large Millimeter Array (ALMA) has swung open new discovery space in almost every area of astrophysics. Its unparalleled sensitivity to tracers of gas and dust emission, both in the nearby and distant Universe, have been revolutionary: from intricate gaps in protoplanetary disks around young stars (e.g. ALMA Partnership et al. 2015; Andrews et al. 2016), ubiquitous gas outflows from dense cores of nearby galaxies (Leroy et al. 2015; Meier et al. 2015; Ando et al. 2017), the regular detection of molecular gas and dust in normal massive galaxies out to high-redshift (Hodge et al. 2013, 2016; Brisbin et al.

2017), dark matter substructure around massive high- z galaxies (Hezaveh et al. 2013, 2016b,a) to the discoveries of the highest-redshift dusty-star forming galaxies (DSFGs) to-date (Vieira et al. 2013; Strandet et al. 2017; Marrone et al. 2017).

One of the key goals of extragalactic work with ALMA has been the blind survey of the early Universe in dust and gas, to reveal the nature of obscured emission from an unbiased point of view, without the guidance of tracers selected at other wavelengths, primarily the rest-frame ultraviolet or optical. Dust emission can be traced directly in submm/mm continuum, while gas can be traced either indirectly through dust continuum (Scoville et al. 2014, 2016, 2017) or directly through molecular line transitions like CO (Neri et al. 2003; Tacconi et al. 2006, 2008; Casey et al. 2011; Bothwell et al. 2013), which allows a three-dimensional mapping of the Uni-

verse with both spatial and spectral data (Decarli et al. 2014, 2016a,b).

It was never quite clear what would be found with blank-field surveys by ALMA given how few measurements had ever been made previously (and most of those had been done with single-dish submm facilities with much larger beamsizes, obfuscating multi-wavelength counterpart identification; Smail et al. 1997; Barger et al. 1998; Hughes et al. 1998). The potential for groundbreaking discovery was nevertheless high, given our disparate knowledge of the population of galaxies well-studied in the optical and near-infrared, and those discovered at submm/mm wavelengths. The two populations often exhibit completely orthogonal physical characteristics, from their star-formation rates (Chapman et al. 2005; Wardlow et al. 2011; Gruppioni et al. 2013) to their obscuration fractions (Pannella et al. 2009, 2015; Whitaker et al. 2014, 2017), while also exhibiting some troubling degeneracies, like optical color, which can cause one population to seem indistinguishable from another (Goldader et al. 2002; Burgarella et al. 2005; Buat et al. 2005; Howell et al. 2010; Takeuchi et al. 2010; Casey et al. 2014a).

Thus, the first several years of ALMA operation has seen the initial results of the first ALMA blind pencil-beam surveys, including both blank dust-continuum detection experiments (Dunlop et al. 2016; Hatsukade et al. 2016; Aravena et al. 2016b; Franco et al. 2018), molecular gas deep fields (Walter et al. 2016; Decarli et al. 2016a,b), and blank dust-continuum follow-up around specially-chosen protocluster fields (Umehata et al. 2015). One common result among these surveys has been the relative dearth of faint sources discovered at high-redshift ($z > 4$). This paper address why that might be the case, focusing exclusively on galaxies’ dust-continuum emission. We also synthesize results of prior single-dish work and lessons learned about the infrared galaxy luminosity function (the ‘IRLF’) to inform future ALMA deep field campaigns. This paper draws on a complex backward evolution model built to understand and interpret the submm sky, summarized in Casey et al. (2018), hereafter C18. This paper specifically explores the application of this model to ALMA observations. In § 2 we briefly summarize the model setup, § 3 presents the results of the model in comparison with existing ALMA deep fields, § 3.3 presents an alternate analysis of the dust properties of rest-frame UV-selected galaxy populations, and § 4 comments on the potential discriminating power of future ALMA deep surveys for refining constraints on the high- z IRLF. We assume a *Planck* cosmology throughout this paper, adopting $H_0 = 67.7$ km

s^{-1} Mpc $^{-1}$ and $\Omega_\lambda = 0.6911$ (Planck Collaboration et al. 2016).

2. MODEL PARAMETERIZATION

We have built a backward-evolution model to interpret the origins of emission in the submillimeter/millimeter sky from galaxy number counts, redshift distributions and correlations between bands. This model is built to constrain the nature of the IRLF out to high-redshifts, where only small handfuls of dust-obscured sources have been directly characterized. Existing datasets can, nevertheless, inform our interpretation of those epochs through statistical comparisons. A more detailed description of the model’s motivation and structure are provided in C18. We provide only a brief summary here.

The model first constructs an infrared galaxy luminosity function, $\Phi(L, z)$, spanning $0 < z < 12$ with IR luminosities from $10^8 < L < 10^{14} L_\odot$ ¹. At low redshifts this is informed by direct measurements of the IRLF (Sanders et al. 2003; Le Floc’h et al. 2005; Casey et al. 2012b; Gruppioni et al. 2013; Magnelli et al. 2013). At $z \gtrsim 2.1$, we adopt two possible models for the evolution of the luminosity function where it is no longer constrained by data. Both assume $L_\star \propto (1+z)$. Model A assumes a very low number density of DSFGs in the early Universe such that $\Phi_\star \propto (1+z)^{-5.9}$, following the fall-off in bright UV-luminous galaxies at the same epoch, while Model B assumes a much shallower relation, $\Phi_\star \propto (1+z)^{-2.5}$, implying a much higher prevalence of DSFGs in the early Universe. Figure 1, as well as Figure 6 of C18, highlights the differences in the cosmic star-formation rate densities implied by either model; model A (the dust-poor Universe) implies that obscured galaxies might only contribute $\sim 10\%$ toward cosmic star-formation at $z \gtrsim 4$ while model B (the dust-rich Universe) implies that obscured galaxies dominate with $\sim 90\%$ of cosmic star-formation at $z \gtrsim 4$.

The adopted models of the IRLF in C18 fix both the bright-end slope ($\beta_{LF} = -3$) and faint-end slope ($\alpha_{LF} = -0.6$) of the double powerlaw across all epochs. This is done due to our lack of ability to break degeneracies between evolving faint-end slopes and different evolutions in L_\star or Φ_\star . Also, single-dish surveys are largely unable to detect galaxies below L_\star at high- z , and therefore the prescriptions for the faint-end slope are largely irrelevant².

¹ In the model we abbreviate $L_{IR(8-1000\mu m)}$ as L .

² Though sub- L_\star galaxies can be directly detected in the low-redshift Universe, their number density is significantly lower than their high- z cousins, and so they contribute very little to number counts or redshift distributions.

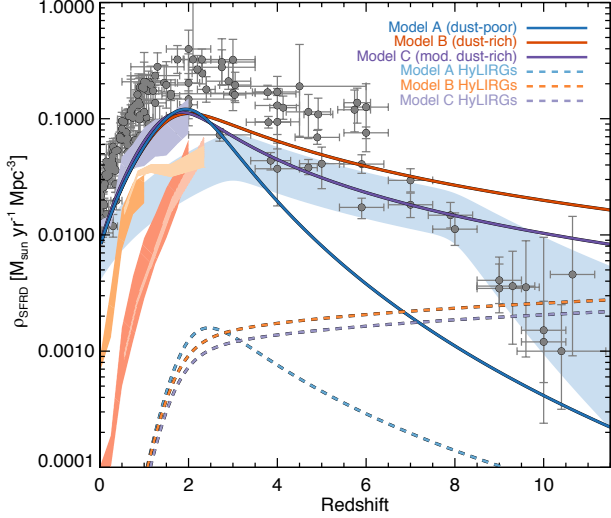


Figure 1. The cosmic star-formation rate density as measured across multiple literature datasets, as summarized in Madau & Dickinson (2014, gray points). The light blue shaded region highlights the total measured contribution of unobscured light (rest-frame UV and optical tracers). Light purple, orange and red transparent regions represent the measured constraints on total obscured contribution, contribution from LIRGs ($10^{11} < L_{\text{IR}} < 10^{12} L_{\odot}$), and ULIRGs ($10^{12} < L_{\text{IR}} < 10^{13} L_{\odot}$), respectively. Thick solid lines illustrate the total contribution from obscured galaxies as proposed by our three models: Model A, the dust-poor early Universe (blue), Model B, the dust-rich early Universe (orange), and Model C, the modified dust-rich early Universe (purple). The contribution of HyLIRGs ($L_{\text{IR}} > 10^{13} L_{\odot}$) to each model is shown in dashed lines to illustrate that Model B and Model C are very similar at the bright-end of the luminosity function.

Beyond the adopted functional form of the luminosity function, our model then assigns an infrared spectral energy distribution ($3\mu\text{m}$ – 3mm) to individual sources according to a probability density function that is dependent on the source’s integrated IR luminosity L and redshift z . SED rest-frame peak wavelengths are a function of L at each redshift, such that more luminous galaxies are intrinsically hotter. We find no significant evidence for an evolution in the L – λ_{peak} relationship. See Figure 3 of C18 and the discussion in § 2.2 for details on how the SEDs are generated. Our SEDs are parameterized via λ_{peak} instead of dust temperature T of the ISM, which makes the model insensitive to different opacity assumptions that impact the relationship between the observable λ_{peak} and the physical quantity³ T . How-

³ As will be shown in Figure 8, optically thin vs. optically thick assumptions can dramatically impact a galaxy’s SED with fixed

ever, the impact of heating from the cosmic microwave background (CMB) at very high redshifts is a strong function of the underlying physical dust temperature T (da Cunha et al. 2013). As in C18, and informed by the rough luminosity sensitivities of ALMA deep field surveys shown in Figure 2, we continue with the assumption that SEDs transition from optically thick to thin with $\tau = 1$ at $100\mu\text{m}$.

With luminosity functions and SEDs in-hand, sources are then injected into mock maps at any wavelength along the SED. A mock map consists of a regularly-spaced grid with pixel size equal to 1/5 of the minimum beamsize FWHM simulated; positions of injected sources are randomly assigned. In C18, we investigated the characteristics of maps spanning the IR through millimeter, from $70\mu\text{m}$ through 2mm . Once all sources at all redshifts have been injected into these mock maps, they are convolved with the beamsize of observations specific to a certain instrument at a certain observatory, instrumental noise is added to the maps, and sources are re-extracted to compare against real observations.

In this paper, we draw up mock ALMA deep field maps in band 6 using the quoted beamsizes and RMS noise values of ALMA campaigns—though small adjustments to the beamsize are negligible since our maps are not confusion-limited. Since we do not model the galaxies’ sizes directly, and instead input them as point sources, adjustments to the angular resolution on the order of $0.5''$ – $2''$ do not change our results, but we do note that sources extended on $>0.5''$ are somewhat common (Hodge et al. 2016) and the potential to resolve sources at higher angular resolution should be taken into account for designing future observational campaigns. In addition to the modeled 1.2mm maps (band 6), we simulate hypothetical maps at $870\mu\text{m}$ (band 7), 2mm (band 4) and 3mm (band 3) to interpret what role they might play in constraining dust emission at high- z . Table 1 lists the observational setups we test in this paper, and Figure 2 shows the rough luminosity limits of these flux density thresholds in the four ALMA bands. Figure 3 shows mock maps at all sample wavelengths given each setup.

2.1. Importance of the Faint-End Slope of the IRLF

It is clear from a number of quick tests on the C18 model that it is α_{LF} , the faint-end slope of the luminosity function, that has the most profound and dominating

dust temperature. This motivates our focus on rest-frame peak wavelength, λ_{peak} , instead of dust temperature itself. While the observables might change substantially at a fixed temperature, they do not for a fixed λ_{peak} .

Table 1. Characteristics of Observational Setups

PASSBAND	INSTRUMENT/ TELESCOPE	BEAMSIZE FWHM ["]	RMS [μ Jy]
870 μ m	ALMA BAND 7	0.5 \times 0.5	25
1.2 mm	ALMA BAND 6	0.6 \times 0.6	13
2 mm	ALMA BAND 4	1.0 \times 1.0	6
3 mm	ALMA BAND 3	1.5 \times 1.5	3

Notes. This table summarizes the different observational setups we test for on 1–400 arcmin² scales in our ALMA-focused simulations. The chosen beamsizes and RMS values are typical of observations available in the ALMA archive at each frequency.

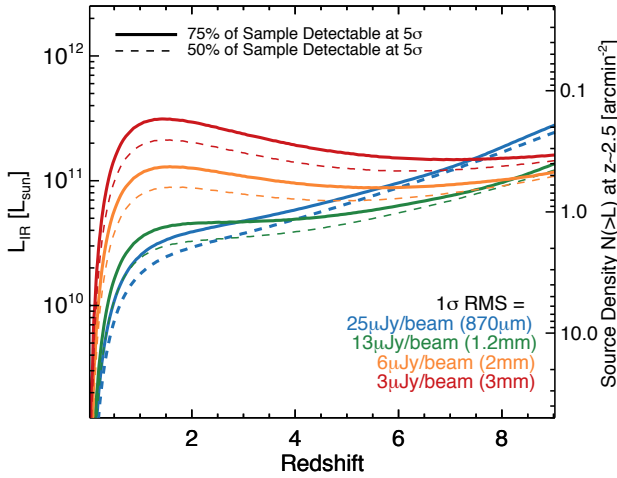


Figure 2. The luminosity sensitivity limits of four different ALMA deep field surveys, with 1σ RMS depths of $25\mu\text{Jy}/\text{beam}$ (at $870\mu\text{m}$, blue), $13\mu\text{Jy}/\text{beam}$ (at 1.2mm , green), $6\mu\text{Jy}/\text{beam}$ (at 2mm , orange) and $3\mu\text{Jy}/\text{beam}$ (at 3mm , red) as outlined in Table 1. Line type denotes what fraction of the population at the given luminosity and redshift would likely be detectable above the given threshold: $>75\%$ (solid) or $>50\%$ (dashed). The curves are determined by the observed $L_{\text{IR}} - \lambda_{\text{peak}}$ relationship (see Figure 3 of C18) with typical 10% scatter. At high-redshifts we incorporate the impact of CMB heating (da Cunha et al. 2013) on luminosity detection limits, which effectively flattens out the dramatic negative K-correction seen in the millimeter beyond $z \sim 6$. The right y-axis is labeled with the approximate source density of sources above a given luminosity on the sky at $z \approx 2.5$. We discuss the important trade-offs of survey area vs. depth later in the paper.

effect on the density of sources in 1.2mm ALMA deep fields. Because this paper focuses on these deep fields, which probe a bit deeper than the single-dish results summarized in C18, we expand on the C18 models A and B in this paper by also testing different values for α_{LF} .

In Figure 4, we show the results of adjusting the value of the faint-end slope (within $-1 < \alpha_{\text{LF}} < -0.1$) for both Models A and B. All other parameters in the models are fixed to the values as given in Table 3 of C18. This figure shows the number of detected sources above 3.5σ significance with a $35\mu\text{Jy}$ RMS as a function of α_{LF} (these values follow the specifications of Dunlop et al. 2016, where 47 sources are identified above this threshold in a 4.4arcmin^2 map). At a fixed value of α_{LF} , we constrain the number of expected sources and its uncertainty by using 100 Monte Carlo simulations for either Model A or Model B. At fixed α_{LF} , Model A will produce 30% fewer sources than Model B, directly attributable to the different adopted values of ψ_2 , the parameter determining the high- z evolution of Φ_* . This indicates that $\sim 70\%$ of sources in our simulated maps are likely to sit at redshifts unaffected by model differences, mainly $z < 2$. We explore this more fully in the next section. The values of α_{LF} that result in best agreement with the HUDF source density are $\alpha_{\text{LF}} = -0.69^{+0.06}_{-0.07}$ for Model A and $\alpha_{\text{LF}} = -0.49^{+0.07}_{-0.06}$ for Model B.

In what follows, we analyze a few different permutations of the models as a result of the impact of the faint-end slope of the luminosity function. For illustrative purposes, we continue our analysis of Model A and Model B exactly as given in C18, fixing the faint-end slope to $\alpha_{\text{LF}} = -0.6$. In addition, we also provide analysis of Model A with its best-fit value of $\alpha_{\text{LF}} = -0.69$ and Model B with its best-fit value of $\alpha_{\text{LF}} = -0.49$. We also introduce a Model C in this paper, which is a modification of the dust-rich Model B. The only change from Model B is that Model C allows the faint-end slope to evolve with redshift like:

$$\alpha_{\text{LF}} = \begin{cases} \alpha_0(1+z)^{a_1} & : z \ll z_{\text{turn}} \\ \alpha_0(1+z)^{a_2} & : z \gg z_{\text{turn}} \end{cases} \quad (1)$$

Physically, this model is motivated by the observed steepening of the rest-frame UV-slope towards the highest redshifts (Bouwens et al. 2007, 2015; Reddy & Steidel 2009; McLure et al. 2013; Finkelstein et al. 2015) and also in the steepening of the low-mass end of the stellar mass function (Grazian et al. 2015; Duncan & Conselice 2015; Song et al. 2016). The IRLF might logically exhibit the opposite behavior by flattening at increased redshift. In other words, this promotes the idea that low-mass galaxies should be less dust-enhanced at earlier redshifts than at later redshifts. Following the methods of C18, the adopted functional form is then dependent on $x \equiv \log_{10}(1+z)$, $x_t = \log_{10}(1+z_{\text{turn}})$ and

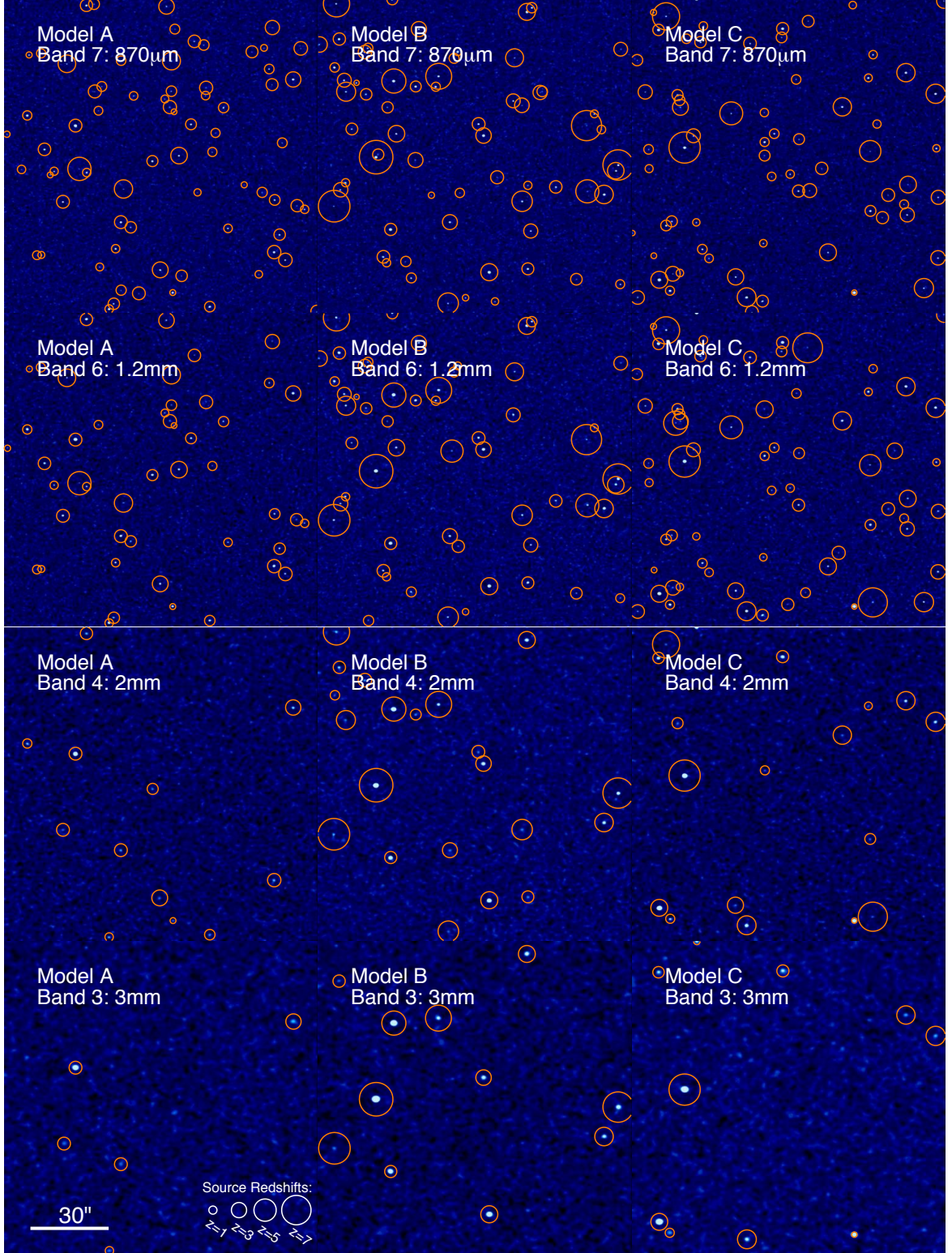


Figure 3. $2' \times 2'$ cutouts of mock ALMA maps at $870\mu\text{m}$ (Band 7; top row), 1.2 mm (Band 6; second row), 2 mm (Band 4; third row) and 3 mm (Band 3; last row). The left column represents the output from Model A, the dust-poor Universe model. The middle column is the output from Model B, and the right column from Model C; both Models B and C represent a dust-rich Universe model, with different prescriptions for the faint-end slope of the luminosity function. The assumed RMS noise values for these maps are given in Table 1. Sources detected at $>5\sigma$ significance are encircled in orange in all maps; for illustrative purposes, the circle size is proportional to injected source redshift (a legend is given in the low left panel). The full redshift distributions for all samples is given in Figure 10.

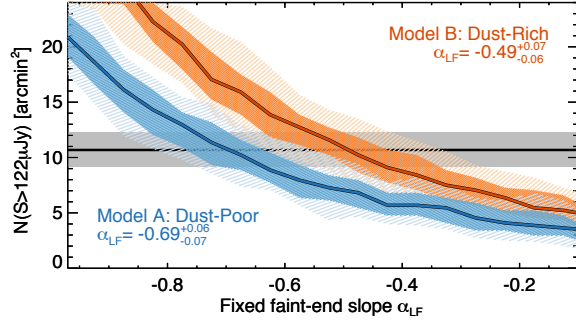


Figure 4. The number of sources per arcmin² found in our simulated maps as a function of the faint-end slope of the luminosity function, α_{LF} . The black horizontal line and gray error region denotes the measured number of sources per square arcminute in the Dunlop et al. (2016) 4.4 arcmin² HUDF map; 47 sources were identified above a 3.5σ significance with a 1σ RMS of $35\mu\text{Jy}$. At a fixed value of α_{LF} we simulate 100 such 4.4 arcmin² maps and identify the number of $>3.5\sigma$ sources. The blue line and error region show the results of Model A, the dust-poor early Universe, while the orange line denotes the results of Model B, the dust-rich early Universe. C18 assumes a fixed faint-end slope of $\alpha_{LF} = -0.6$, while here we measure best agreement with the HUDF dataset if $\alpha_{LF} = -0.69^{+0.06}_{-0.07}$ for Model A and $\alpha_{LF} = -0.49^{+0.06}_{-0.06}$ for Model B.

$x_w = z_w/(1 + z_{\text{turn}})$, where $z_w \equiv 2.0$, such that:

$$\begin{aligned} \log \alpha_{LF}(x) = & -\frac{(a_2 - a_1)x_w}{2\pi} \left[\ln \left(\cosh \left(\pi \frac{x - x_t}{x_w} \right) \right) \right. \\ & \left. - \ln \left(\cosh \left(-\pi \frac{x_t}{x_w} \right) \right) \right] \\ & - \frac{(a_2 - a_1)}{2} x - \log(-\alpha_0) \end{aligned} \quad (2)$$

For Model C we adopt all of the same parameters as Model B of C18 (e.g. $z_{\text{turn}} = 1.8$, $z_w = 2.0$). While Model B would have both a_1 and a_2 set to zero in Equations 1 and 2 we set $a_1 = 0$ and $a_2 = -0.7$ to accommodate a flattening of the faint-end of the luminosity function at high-redshift. We set $\alpha_0 = -0.69$ at $z = 0$, in line with the measured best-fit value for Model A from Figure 4.

In summary, we analyze the results of three different model universes in this paper. The first is Model A, the dust-poor Universe model, that assumes very few DSFGs beyond $z > 4$, while the second is Model B, the dust-rich Universe model, that assumes DSFGs make up $\sim 90\%$ of the cosmic star-forming budget at $z > 4$. Both models A and B explore different values of α_{LF} , either fixed to -0.6 as in C18 or, for most analysis in this paper, adjusted to the best-fit data-driven value as found in Figure 4. The variation of α_{LF} values motivates the introduction of Model C. Model C is a modi-

fied version of Model B; mainly, it proposes a dust-rich early Universe with high prevalence of DSFGs at high-redshifts, but fewer and fewer lower luminosity DSFGs with increasing redshifts resulting in a flatter slope to the IRLF. Note that all three models provide plausible fits to the number counts of galaxies at higher flux densities as measured from single-dish surveys (see C18).

3. COMPARISON TO EXISTING 1.2 MM DATASETS

ALMA deep fields have extended our knowledge of millimeter number counts into the sub-mJy regime, not probed by prior datasets. These ALMA deep field efforts include:

- SSA22 Core Deep Field (Umehata et al. 2015): a 4.5 arcmin^2 1.1 mm survey of the $z \sim 3.09$ protocluster core to a depth of $70 \mu\text{Jy}/\text{beam}$ with a $0.53 \times 0.50''$ beam,
- The Hubble Ultra Deep Field (HUDF; Dunlop et al. 2016): a 4.5 arcmin^2 1.3 mm survey with $0.7''$ beam to a depth of $35 \mu\text{Jy}/\text{beam}$,
- The SXDF ALMA Deep field (Hatsukade et al. 2016): a 2.0 arcmin^2 survey at 1.1 mm to a depth of $\sim 55 \mu\text{Jy}/\text{beam}$,
- The ASPECS Pilot Deep field (Walter et al. 2016; Aravena et al. 2016a): a 0.79 arcmin^2 1.2 mm deep field to a continuum depth of $12.7 \mu\text{Jy}/\text{beam}$ and a $1.5 \times 1.0''$ beam. ASPECS also mapped the same region in 3 mm continuum, which achieved a 1σ RMS of $3.8 \mu\text{Jy}/\text{beam}$ with a $2 \times 3''$ beam, and
- The GOODS-ALMA Survey (Franco et al. 2018): a 69 arcmin^2 1.1 mm deep field centered on CANDELS, containing the HUDF pointing of Dunlop et al. mapped to an RMS of $0.18 \text{ mJy}/\text{beam}$ analyzed with a synthesized beam of $0.6''$ but originally mapped at high spatial resolution with a beamsize of $0.2\text{--}0.3''$.

Further observational efforts are currently underway, primarily the cycle 4 ASPECS large program intended to cover an area of 4.6 arcmin^2 to a depth similar to the ASPECS pilot survey. This would significantly deepen the HUDF pointing; note that the ASPECS-Pilot, HUDF, and GOODS-ALMA surveys are all sequentially nested in the same patch of sky centered on the HUDF. Several additional projects have combined results from archival ALMA datasets to infer deep (sub)millimeter number counts, including Ono et al. (2014) who measure number counts at 1.1–1.3 mm down to 0.1 mJy covering an area of 3 arcmin^2 across 10 different fields, Carniani et al. (2015) who measure number counts down to 0.1 mJy across 18 different fields from

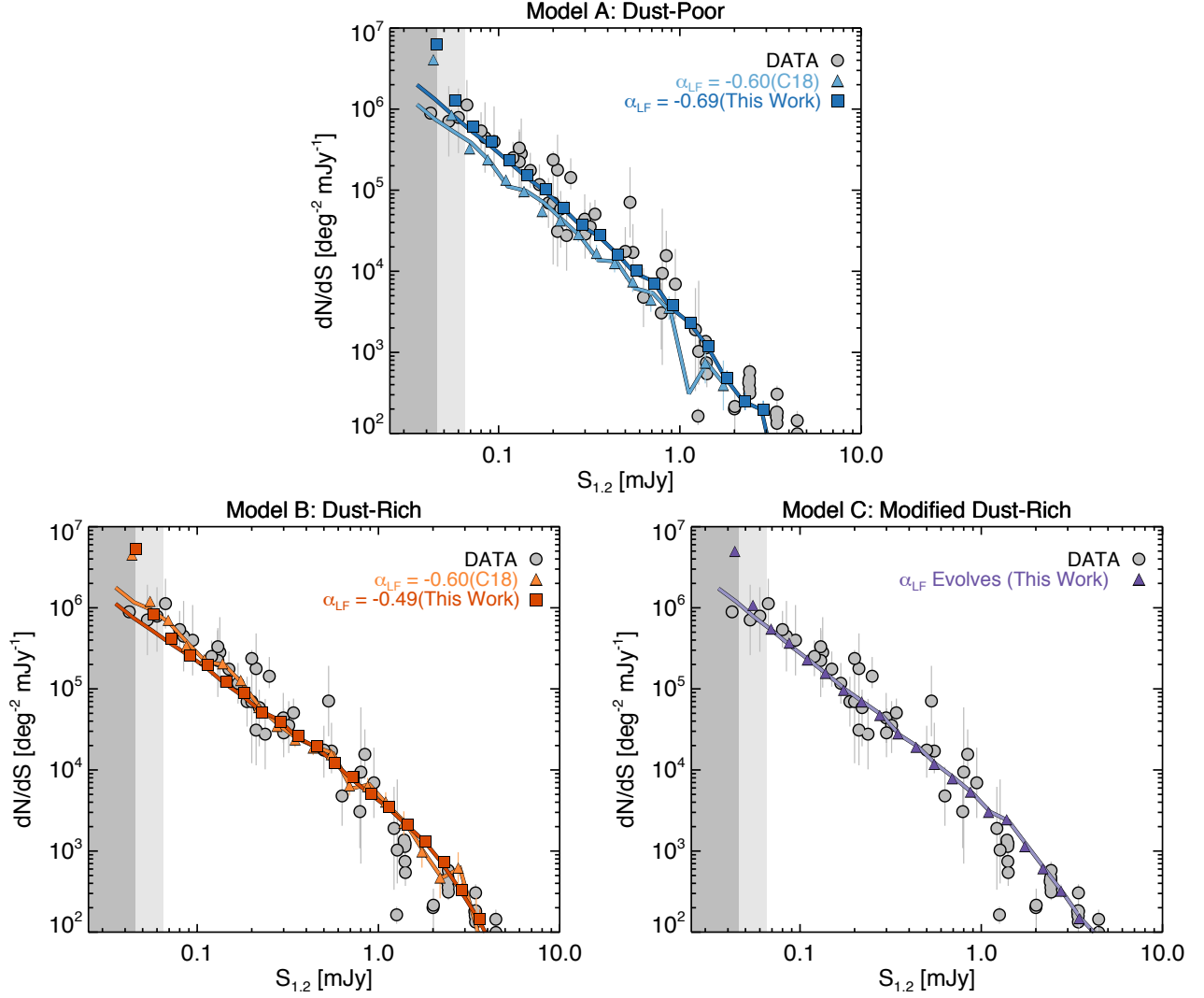


Figure 5. A comparison of 1.2 mm number counts from the literature (gray points; Ono et al. 2014; Carniani et al. 2015; Dunlop et al. 2016; Hatsukade et al. 2016; Aravena et al. 2016b; Fujimoto et al. 2016; Oteo et al. 2016; Franco et al. 2018), and our simulations output. Sources are extracted down to 3.5σ significance; the dark gray region represents flux densities at $<3.5\sigma$, while the light gray region represents sources with $3.5 < \sigma < 5$. The contamination rate below 5σ exceeds 10%, and so we advocate for analysis of individual systems only above 5σ . At top, we show the family of models that assume a dust-poor early Universe, with $\Phi_* \propto (1+z)^{-5.9}$ (Model A). Below, we assume a dust-rich early Universe with $\Phi_* \propto (1+z)^{-2.5}$ (Model B and Model C). Both Model A and Model B assume a fixed faint-end slope of the luminosity function ($\alpha_{LF} = -0.6$) as in C18 (triangles), and then re-measure the number counts using the best-fit faint-end slope as measured in Figure 4 (squares). Model C is a variant of Model B where α_{LF} is allowed to evolve such that the IRLF slope at the faint end becomes shallower with increasing redshift. All injected source counts are shown as solid lines, while extracted source counts shown as symbols (triangles or squares). This figure shows that all models (A–C) agree with measured number counts at 1.2 mm – despite quite significant differences in assumed number density of high- z dusty galaxies.

the archive ($\sim 4 \text{ arcmin}^2$), Fujimoto et al. (2016) who combined data spanning 10 arcmin^2 of various depths at 1.1 mm, and Oteo et al. (2016), which describes the ALMACAL project, which uses data from the regions around commonly-used ALMA calibrators to produce deep maps at $870 \mu\text{m}$ ($\sim 6 \text{ arcmin}^2$) and 1.1 mm ($\sim 16 \text{ arcmin}^2$). Because the vast majority of data collected is from ALMA band 6 (1.1–1.3 mm), we restrict our comparative analysis to the band 6 datasets.

Figure 5 shows a detailed comparison of measured number counts at 1.2 mm from these literature resources against our three models. The solid lines indicate the injected source number counts, while the colored symbols are the output extracted number counts. There is remarkable global agreement of the measured number counts from ALMA and the model output, even in the case of the fixed $\alpha_{LF} = -0.6$ models from C18, despite the fact that these models were generated to fit

luminosity functions of much brighter sources found in single-dish surveys only. Unfortunately the measured number counts are highly uncertain and susceptible to cosmic variance due to small number statistics in small, pencil-beam surveys. It is not even immediately obvious that the adjustments made to the faint-end slope of the luminosity function have made a discernible difference with such substantial scatter from the data themselves.

3.1. Completeness, Contamination, and Sample Cleaning

Note that the final sample sizes of the [Dunlop et al.](#), [Aravena et al.](#) and [Franco et al.](#) works were 16, 9, and 20 respectively. Our models predict anywhere between 31–47, 21–38, or 85–146 for the given areas, depths, and detection thresholds, respectively. There is some tension in these estimates, despite no disagreement between their calculated 1.1–1.3 mm number counts and our model results (shown in Figure 5). Here we explore reasons for this tension in their final source lists.

We caution that disagreement between our model predictions (31–47) and the [Dunlop et al. \(2016\)](#) statistics (16 sources) are likely caused by the additional cuts that [Dunlop et al.](#) make to reduce their original sample of 47 detections above a 3.5σ threshold to 16 with OIR counterparts. These cuts are motivated by the estimated contamination rates from spurious sources at the 3.5σ detection threshold. The raw number of $>3.5\sigma$ sources found in [Dunlop et al.](#) is in agreement with our predictions.

Our predictions for the ASPECS-Pilot 0.79 arcmin^2 map (21–38 sources predicted) are discrepant with observations (9 sources observed). This tension could be quickly alleviated by adopting a shallower faint-end slope to the IRLF or by invoking cosmic variance on such small areas ($<1 \text{ arcmin}^2$). Even small variations in the faint-end slope α_{LF} can have profound effects on the predicted source counts in such a small, deep drill survey. For example, adopting $\alpha_{\text{LF}} = -0.6$ (instead of -0.69) for Model A results in a predicted number of sources 40% lower in a mock ASPECS-Pilot map. If we modify the detection threshold to 5σ , up from 3.5σ , we note that our predictions, of detecting 5–12 sources, fall more in line with the observed 5 sources. Indeed, we find the signal to noise threshold to be rather impactful on the estimated source contamination rates.

We estimate contamination in our simulations in two ways. First, we invert the maps and run our source detection algorithm on the negative image, where we know all detections will be false. This is an often used analysis technique for real data, where simulations like ours are not immediately available. It should come as

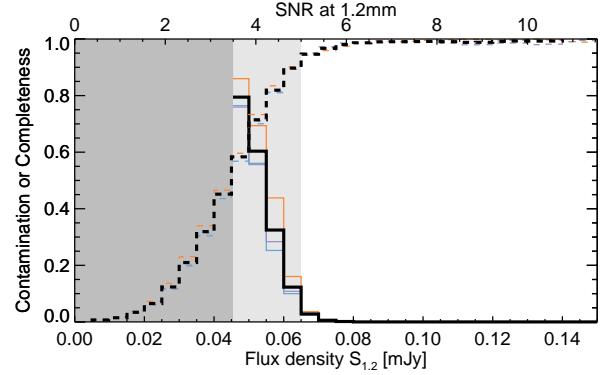


Figure 6. The measured contamination (solid lines) and completeness (dashed lines) for our simulated 1.2 mm ALMA maps. The colored lines indicate individual simulations with different model assumptions, following the same color scheme as other plots in this manuscript. We do not find any variation by model parameters because these maps are not confusion limited. The average contamination and completeness for all simulations is shown in black. We find that sources with $3.5\sigma < \text{SNR} < 5\sigma$ are potentially very highly contaminated by positive noise fluctuations, and similarly, suffer from $>10\%$ incompleteness.

no surprise (and is indeed reassuring) that our detection rate for inverted sources is uniform across all of our models; we estimate a false rate of 4.6 ± 0.6 sources per arcmin^2 . [Dunlop et al.](#) find 29 such spurious sources in their 4.4 arcmin^2 map, which is in 3σ tension with our findings, though they also offer other calculations which estimate ≈ 20 false sources. Twenty false sources above $>3.5\sigma$ would be in perfect alignment with our model output. In the case of the ASPECS-Pilot project, we estimate 3.6 ± 0.5 false sources in their 0.79 arcmin^2 (out of the 9 sources above 3.5σ). If we consider the two of their sources without OIR counterparts as possible contaminants, this agrees nicely within Poisson uncertainty. However, it does not preclude other false identifications in the [Aravena et al. \(2016b\)](#) sample.

As a more robust test and one lending itself to the full information available in our model, we also estimate the contamination and completeness of our simulations by comparing the list of injected sources with the list of detected sources. For simplicity we assume galaxies are point sources, unresolved on all spatial scales of our simulations. Figure 6 shows both completeness and contamination rates as a function of flux density and signal-to-noise. Contamination (per bin) is the fraction of sources in the output catalog at that flux density which lack corresponding input sources within a beam-size of the source centroid. Completeness is the number of sources (per input flux density) that are identified at any significance $>3.5\sigma$ in the output catalog. It is some-

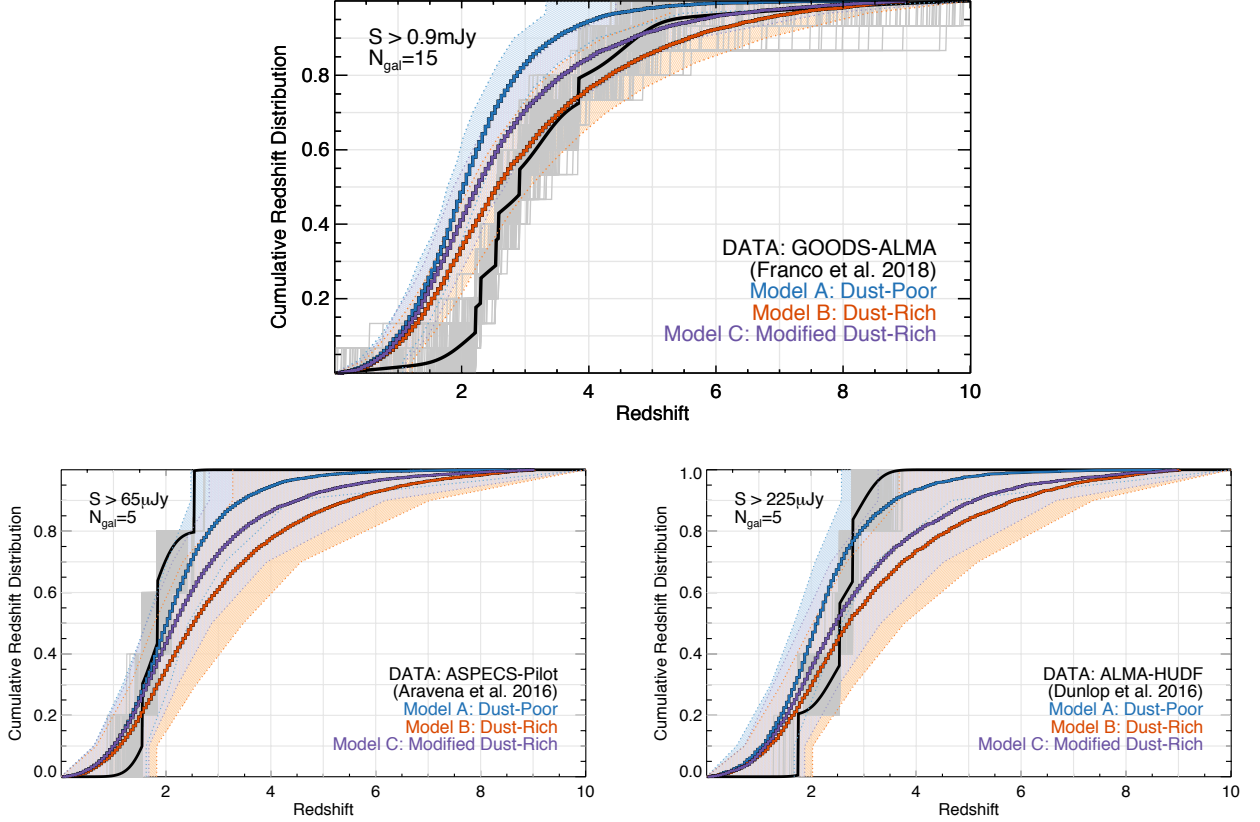


Figure 7. Comparison of measured redshift distributions of $>5\sigma$ sources in the 1.2mm ASPECS-Pilot sample (Aravena et al. 2016a), the 1.3mm HUDF sample (Dunlop et al. 2016) and the 1.2mm GOODS-ALMA sample (Franco et al. 2018) against our three models: the dust-poor Model A (blue), the dust-rich Model B (orange) and the modified dust-rich Model C (purple). Redshifts are a mix of photometric and spectroscopic redshifts. The gray (data), and light shaded regions represent the uncertainty distributions given the sample size of ASPECS (5 galaxies), HUDF (5 galaxies), or GOODS-ALMA (15 galaxies) in addition to redshift uncertainty for the subsample. Small deviations in the faint-end slope of the luminosity function does not impact the measured redshift distribution significantly (i.e. the difference between $\alpha_{\text{LF}} = -0.6$ and $\alpha_{\text{LF}} = -0.69$ for Model A is indiscernible, though it does impact the total number of sources identified above the significance threshold, as shown in Figure 4). These samples limited by small number statistics are not large enough to distinguish between competing models. In addition, the GOODS-ALMA analysis could be biased against low-redshift sources that are probably larger and resolved out of the map.

what concerning that the expected contamination rate is above 10% below $\text{SNR} = 5$. As noted also in Dunlop et al., the high contamination rate at $3.5 < \sigma < 5$ (compared to single-dish results) is likely due to the incredibly high number of independent beams in ALMA maps. Therefore we advise future ALMA deep field programs to consider sources at lower SNR ($3.5\sigma < \text{SNR} < 5\sigma$) cautiously. It is even a possibility that a positive spike in the ALMA map could correspond with an OIR counterpart accidentally; we measure this type of accidental counterpart identification at the level of $\sim 9\%$ above $F125W < 28$ (using the HUDF photometric catalog from Rafelski et al. 2015).

In contrast to the Aravena et al. and Dunlop et al. results, the tension between our estimates (85–146) and the Franco et al. (2018) results (20 sources) requires an

analysis of angular resolution. There is some added complication due to their data acquisition in an extended baseline mode (achieving a native resolution of ~ 0.2 – $0.3''$). This could, in principle, lead to a lower detection rate because sources larger than these spatial scales could be resolved out of the mosaic. To counter this effect, the authors taper the map to a resolution of $0.6''$ with the intention of recovering any missed extended sources in the original mosaic⁴ in addition to reducing the number of independent beams that cause excess source contamination at low SNR thresholds. While the tapered map does recover some missed sources, Franco

⁴ Indeed, of the 20 sources identified in their tapered $0.6''$ map, only 14 are found in the higher resolution images.

et al. then further discuss the effects of galaxy size on detectability in the tapered map. They find a very high completeness for point sources, but a drastically lower completeness for galaxies of even modestly larger sizes (with FWHM ranging 0.2–0.9"). Using the Hodge et al. (2016) measurements of DSFGs from ALESS as a benchmark, we estimate ~ 1 mJy sources might have typical FWHM sizes of 0.4–0.5", resulting in 75–95% incompleteness. Indeed, their estimated cumulative number counts for sources with $S_{1.1} > 0.7$ mJy gives 61^{+50}_{-58} sources that should be found in the map (contrasting with the 20 sources found). This is in-line with our predictions of 85–146 sources from Models A–C. It is worth reiterating that our simulations input all galaxies as unresolved point sources. The Hodge et al. work highlights that even the 0.6" tapered map is at risk of resolving sources, leading to further source incompleteness. This emphasizes the importance of more compact ALMA configurations (with larger beamsizes) to conduct such blind deep field surveys.

3.2. Redshift Distributions

However uncertain, the rate of false detections is critical to the interpretation of the 1.2 mm ALMA-detected redshift distributions and the answer to the question of why there are so few high- z galaxies detected in ALMA deep fields. In this section we explore the predicted and measured redshift distributions for 1.2 mm samples. We first compare against the Aravena et al. (2016a) and Dunlop et al. (2016) samples, and then follow with a discussion of the Franco et al. (2018) sample.

While both the Aravena et al. (2016a) and Dunlop et al. (2016) analyses includes sources identified down to a significance of 3.5σ , our analysis suggests that 40–80% of sources at that significance are spurious. Unfortunately, the existing maps contain very few high significance sources, and a detection threshold of 5σ leaves us with five sources in each data samples. One high significance source is in both the Aravena et al. (2016a) and Dunlop et al. (2016) samples⁵, leaving us with only nine unique sources identified at $>5\sigma$. Nevertheless, includ-

ing sources found at lower significance could substantially contaminate the analysis of source redshift distributions, and so we choose to only compare with the most robust subset.

The comparison with the Franco et al. (2018) work is in some ways more straightforward, because the sample is larger, but more complex because there is an additional selection bias folded into the comparison: we know that galaxies that are more extended in their millimeter emission are more likely to be excluded from the sample. The implications of this bias on the redshift distribution are unclear. Of the 20 galaxies identified in their map, we compare the redshift distribution of 15 of those to our models, with flux densities $S > 0.9$ mJy (representing a 5σ detection threshold with a 0.18 mJy RMS). It could be argued that low redshift galaxies might be physically larger (and thus subtend larger angles, despite the roughly constant angular diameter distance beyond $z \sim 1$; van der Wel et al. 2014). Thus they might be preferentially filtered out due to their size, being extended on spatial scales $\sim 1''$. However, this trend of increased size at lower-redshift has not been shown conclusively in dust continuum tracers; the best measurements to-date contain ~ 20 galaxies (Hodge et al. 2016) that also might be impacted by a luminosity and dust-temperature bias.

Despite the small number of sources available for comparison (5, 5, and 15 in the three nested maps), we can compare the shape of the cumulative redshift distribution for these unequivocal, reliable detections with our model output to see if they broadly agree. Figure 7 presents these comparisons. The comparison is a bit unfair, given that we are limited to a handful of galaxies in each sample and our model is representative of thousands of sources detected over several tens of arcmin². For this reason, we illustrate the model uncertainty randomly drawing many subsets of sample size $n = 5$ or $n = 15$ from our large simulated sample. The shaded regions on Figure 7 represent the inner 68th percentile of those subsets. The gray curves represent Monte Carlo draws of the data from a cumulative redshift probability distribution for each of the five (or 15) galaxies in each sub-sample, incorporating errors due to photometric redshifts.

It is clear from these plots and the associated uncertainty that current datasets are not constraining or able to distinguish between models. The comparison with Franco et al. (2018) in particular does show a deficit of low-redshift sources, which could be attributable to the high angular resolution of the observations, although that is yet unclear.

⁵ This source is UDF3 in Dunlop et al. and C1 in Aravena et al. at 03:32:38.53–27:46:34.6, at a redshift of $z = 2.543$. Somewhat concerning is the discrepancy between reported flux density measurements, with UDF3 reported to have a 1.3 mm flux density of $863 \pm 84 \mu\text{Jy}$, while C1 reported to have a 1.2 mm flux density of $553 \pm 14 \mu\text{Jy}$. Though the frequency of observations was not identical between these two programs, the 1.2 mm flux density should be either equal to or greater than the 1.3 mm flux density, due to the shape of galaxies' SEDs on the Rayleigh-Jeans tail of cold dust emission. One might expect such a galaxy at $z = 2.5$ to have a flux ratio of $S_{1.2}/S_{1.3} = 1.3$, though the measured ratio is $S_{1.2}/S_{1.3} = 0.64 \pm 0.10$.

If any conclusions can be drawn from this redshift distribution analysis, it is that the apparent lack of very high-redshift detections in ALMA deep field pointings to-date are a direct result of the limiting survey area (the fact that they have only been pencil-beam surveys), depth, and the intrinsic property of the IRLF that is known at least out to $z \sim 2$ directly, and through this work more indirectly: that the faint-end slope α_{LF} is shallow. As a result of the shallow faint-end slope, the expected redshift distributions for 1.2 mm surveys of this size is between $1.7 < \langle z \rangle < 3.5$. Samples of tens to hundreds of $>5\sigma$ detected sources are needed to make distinctions between models (and we discuss possible observational strategies for doing this in more optimal bands later in § 4).

3.3. Analysis of UV-bright Population

An alternate approach to the interpretation of ALMA deep fields is to analyze expected detection statistics of UV-selected galaxies already identified in the field of view. In this section we focus on the analysis of Bouwens et al. (2016), hereafter B16, who present a sample of 35 Lyman Break Galaxies (LBGs) which they expected to detect in the ASPECS-Pilot map of Aravena et al. (2016a) as well as the analysis of Capak et al. (2015) who present 12 rest-frame UV-selected galaxies at $z \approx 5.5$ with dust continuum observations. Both of these works argue that high-redshift LBGs might be relatively dust-poor compared to lower redshift ($z \sim 2$) analogues because their ratio of IR-to-UV luminosity is lower at a given rest-frame UV color.

With only seven sources detected with OIR counterparts in the ASPECS-Pilot map⁶, Bouwens et al. conclude that the most reliable way of estimating dust emission in high- z galaxies is by scaling their stellar masses, not using their rest-frame UV colors that would have predicted 35 detections by their calculations. While other studies often make use of the IRX- β relationship – the relationship between the ratio of IR to UV luminosity ($\text{IRX} \equiv L_{\text{IR}}/L_{\text{UV}}$) to the rest-frame UV spectral slope, β – to infer dust luminosity, Bouwens et al. argues that using that method can dramatically over-predict mm-wave flux densities for individual rest-frame

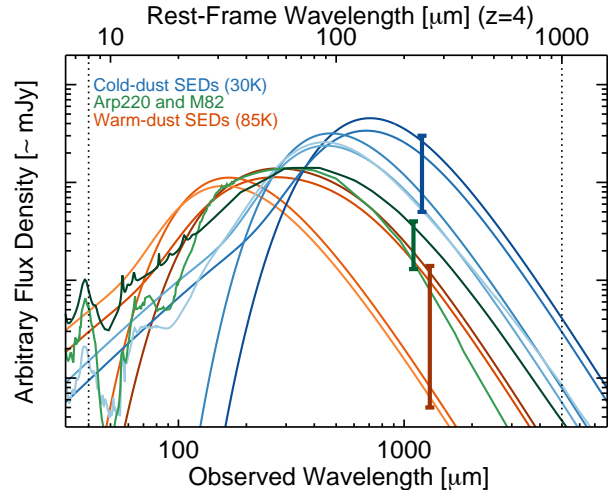


Figure 8. Here we show a set of SEDs for a $z = 4$ galaxy all with the same integrated IR luminosity between 8–1000 μm in the rest-frame. All five blue curves adopt a cold-dust temperature (in this case 30 K). Variation among the cold-dust SEDs is due to: inclusion or not of a mid-infrared powerlaw component, and whether or not the SED is assumed to be optically thin at all wavelengths (those that are peak at shorter rest-frame wavelengths than those assumed to be optically thick to $\lambda \approx 100 \mu\text{m}$). We also include comparison SEDs for both Arp 220 and M82 as local examples of galaxies with intrinsically warm dust SEDs (green curves, Arp 220 slightly darker of the two). The warm-dust SEDs shown in the orange curves assume a dust temperature of 85 K; the variation is, again, due to opacity assumptions and to a lesser extent, to inclusion of an even hotter-dust mid-infrared powerlaw. Observed 1.1–1.3 mm flux densities for these $L_{\text{IR}}=10^{12} L_{\odot}$ SEDs are shown with vertical lines, ranging over two decades in flux density.

UV-selected galaxies⁷, this based on the low rates of detection for LBGs in the ASPECS-Pilot map. Adopting a stellar mass predictor for $S_{1.2}$ instead, Bouwens et al. suggest that this can be used across a range of redshifts (to beyond $z \gtrsim 4$) as long as there is a monotonic change in galaxy SEDs with redshift, such that they increase in dust temperature, suggesting $T_{\text{dust}} \propto (1+z)^{0.32}$. The evolution in dust temperature is deemed necessary to account for lower perceived flux densities on the Rayleigh-Jeans tail of blackbody emission for high- z galaxies compared to those at low- z .

Here we provide an alternate interpretation from B16, suggesting instead that the functional form of the adopted SED and reference IRX- β relationship matter

⁶ Seven sources are found with OIR counterparts in Aravena et al. (2016b), although only three of those sources overlap with the list of 35 LBGs analyzed in B16. B16 quotes that six LBGs are tentatively detected (including those three $>3.5\sigma$ sources) by pushing the significance threshold down to 2σ . Four of the seven $>3.5\sigma$ detections are not included in the B16 LBG samples as they sit at lower redshifts.

⁷ On this point, we agree with Bouwens et al. (2016) that scaling from IRX- β can dramatically over-predict mm-wave flux densities, although we caution that the SED assumptions made by Bouwens et al. could be improved upon further.

a great deal to the interpretation of galaxies’ dust luminosities and that no such evolution in dust temperature is necessary to explain the results. The most significant differences between our analyses are:

- Differences in the assumed reference IRX- β relationship: The derived empirical relationship between IRX and β from Meurer et al. (1999) is offset toward bluer-than-intrinsic colors due to differences in aperture sizes of the original measurements.⁸ The aperture-corrected calibration of IRX- β , for the exact same sample of local starburst galaxies, is given in Takeuchi et al. (2012). For given measured values of β and L_{UV} , use of the Meurer et al. curve will result in a factor of ~ 0.3 dex overprediction of L_{IR} in comparison with the Takeuchi et al. relation. This impacts the inferred L_{IR} values in B16 used to predict 1.2 mm flux densities with IRX- β . This discrepancy also impacts the perceived significance of the disagreement between the Capak et al. (2015) sample and the ‘Calzetti’ dust attenuation curve, although some of that tension was reduced by an updated analysis of the rest-frame UV colors in Barisic et al. (2017).
- Differences in assumed SEDs used to map L_{IR} to $S_{1.2}$: B16 explores several types of SEDs but adopts a fiducial 35 K modified blackbody SED to scale between 1.2 mm flux density ($S_{1.2}$) and IR luminosity (integrated 8–1000 μ m) for all UV-selected galaxies. The SEDs we use to map between $S_{1.2}$ and L_{IR} differ primarily because they include a mid-infrared powerlaw component, which can contribute 10–30% to the total IR luminosity of a given galaxy. Physically it comes from much less massive, isolated knots of hot dust heated by discrete sources throughout the galaxy, like OB associations or an AGN (see C18 and Casey 2012, for details). The differences between a modified blackbody and a modified blackbody with a mid-infrared component has an effect such that, for a fixed L_{IR} , the flux densities on the Rayleigh-Jeans tail will be a factor of 0.5–2 \times lower for the latter than the former. In other words, SEDs with a mid-infrared component will have 1.2 mm flux densities a factor of 0.10–0.15 dex

lower than SEDs without the mid-infrared component at matched L_{IR} and SED peak wavelength (λ_{peak}). This discrepancy does not impact the Capak et al. (2015) sample.

- Difference in assumed SED peak wavelength: we also do not assume a single dust temperature (35 K) for the entire sample of LBGs. We emphasize that the 35 K B16 modeled SED peaks at a rest-frame wavelength of $\sim 85 \mu$ m due to the assumption of an optically-thin SED, while we would instead predict rest-frame peak wavelengths in the range of 100–120 μ m for galaxies with SFRs of 1–10 $M_{\odot} \text{ yr}^{-1}$; Figure 8 illustrates some of the dramatic differences in SEDs with the same dust temperature and L_{IR} but different opacity models. For a fixed L_{IR} , the cooler SED that we assume results in a higher predicted flux density by 0.3–0.5 dex at 1.2 mm than the warmer SED assumed by B16, but with the inclusion of the mid-infrared power-law component above, the impact of this SED shift is reduced to 0.15–0.35 dex.

Taking these effects into account and attempting to predict new flux densities for the same set of 35 LBGs analyzed in B16 (three of which are detected at $>3.5\sigma$), our predictions are a factor of 0.1–0.2 dex lower than the predictions quoted in B16. Specifically, using the Takeuchi et al. scaling and our SED assumptions, we would predict 15 of 35 sources detectable at $>3.5\sigma$. Using the SMC attenuation curve (Pettini et al. 1998) and our SED assumptions, the detectable number would drop to 10 of 35. We also test a stellar mass-based predictor of flux density by scaling stellar mass and measured L_{UV} to L_{IR} using the empirical relationship between stellar mass and obscured fraction of star-formation, f_{obs} (Whitaker et al. 2017). Overall, the mass predictor would estimate 14 detections out of the 35. While all of our predictors are off the mark and predict more detections than exist among this sample of LBGs (though SMC-like dust comes closest), we note that there is very little correlation overall between either our predicted flux densities, those of B16, and measured flux densities – a testament to the relative difficulty of inferring galaxies’ dust content or luminosity from stellar emission alone.

Figure 9 shows the inferred IRX- β relationship for the detections (and non-detections) in the ASPECS-Pilot map, in addition to the Capak et al. (2015) sample, with revised UV colors from Barisic et al. (2017). Here, IRX (or the limit thereof) is re-derived for each galaxy in the sample using the observed flux density (or limit thereof) and a family of SEDs deemed most appropri-

⁸ The *IUE* spacecraft measuring the UV luminosity and colors of nearby starburst galaxies had a limited field of view, only able to image galaxies’ cores, while the *IRAS* far-infrared data used to calculate L_{IR} for the same galaxies was unresolved and includes emission on much larger scales. This is discussed extensively in Takeuchi et al. (2012) and Casey et al. (2014b).

ate for the source given its $S_{1.2}$. As discussed in C18, we observe that L_{IR} relates directly to λ_{peak} with some scatter. To predict a IR luminosity from flux density, we generate a family of SEDs (all with a mid-infrared powerlaw component included) that mirror the observed scatter in $L_{\text{IR}} - \lambda_{\text{peak}}$. We then search for all possible SEDs that have the observed flux density at 1.2 mm and use it to generate a probability density distribution in L_{IR} . Then using the measured L_{UV} (with associated uncertainty), we infer IRX and a realistic uncertainty from the single flux density measurement.

Of the seven ASPECS-Pilot sources detected with OIR counterparts, five sit below the canonical IRX- β relationship described by Takeuchi et al. (2012) for blue, compact starbursts, while two are significantly offset above the relation. Non-detections are shown as 3.5σ upper limits. Unlike the results of B16, our results suggest that the vast majority of these upper limits (29/32) are consistent with the Calzetti dust attenuation law. The difference in conclusions is due both to differences in modeled SEDs and reference Calzetti IRX- β relationships.

The IR luminosities of the $z \sim 5.5$ LBG sample (Capak et al. 2015) were fit very similarly to the SEDs in this paper, although lacking the luminosity dependence of λ_{peak} . Note that in this paper we re-derive L_{IR} for the sample using the same method used for the ASPECS-Pilot sample⁹. It is worth noting that the plotted upper limits on IRX in both Capak et al. (2015) and Barisic et al. (2017) are 1σ limits; in Figure 9 we have shown more conservative 3.5σ upper limits. Combined with the shift toward bluer colors as measured by improved rest-frame UV imaging in Barisic et al. (2017), the more conservative IRX upper limits, and the comparison to the Takeuchi et al. curve instead of Meurer et al., the relative tension between the Calzetti dust attenuation law and the $z \sim 5.5$ sample is significantly reduced.

The important finding here – for both the Capak et al. the Bouwens et al. high- z samples – is that this consistency with the Calzetti dust attenuation law cannot be directly ruled out from existing measurements, even with typical SED assumptions that hold for much lower redshift galaxies.

Other works (e.g. Faisst et al. 2017) have argued that there is significant tension between measurements and the Calzetti dust attenuation law for such cold SEDs, and that only much warmer-dust SEDs ≥ 60 K could

ease the tension (whereby warmer-dust SEDs have much lower $S_{1.2}$ for a given L_{IR} than colder-dust SEDs). Faisst et al. (2017) draws on the characteristics of three local galaxy analogues selected from *GALEX* samples as Lyman- α emitters, where all three galaxies have warm dust SEDs with steep Wien tails. In other words, their SEDs are more homogeneously represented by a single luminosity-weighted temperature than a powerlaw distribution of temperatures found in the ISM of typical massive galaxies. We illustrate the difference between our SED assumption and the warmer-dust SEDs in Figure 8; this highlights how a diverse range of SEDs with the same integrated L_{IR} might result in dramatically different measured flux densities on the Rayleigh-Jeans tail.

While our results do not require such hot temperatures to ease tension between measurements and local IRX- β relationships (Calzetti or SMC), we do not wish to completely dismiss the idea that high- z galaxies might have much hotter dust. Indeed, this claim does have some grounding in physical arguments as discussed in Behrens et al. (2018) who present the results of a hydrodynamic zoom-in simulation of a $z \sim 8$ galaxy named Althaea whose luminosity-weighted dust temperature is very warm (91 K, peaking at a rest-frame wavelength of $50\mu\text{m}$), and exhibits a sharp Wien cutoff. They argue that deeply embedded young star clusters might irradiate compact regions of early galaxies' ISM, such that the strong interstellar radiation field leads to much warmer intrinsic temperatures than are seen for more mature galaxies whose ISM might be predominantly more diffuse. They too argue that a Calzetti dust attenuation law can explain the observed characteristics of galaxies like A2744-YD4 at $z = 8.38$ (Laporte et al. 2017), even if the geometry of the dust in such nascent systems is distributed quite differently; but they do so by arguing that this dust is likely much hotter than ~ 30 K.

Though such hot dust is physically plausible in high- z galaxies, our results demonstrate that it is not *needed* to explain the observed dust characteristics of high- z LBG samples. Either warmer temperatures and a steep Wien tail fall-off or a cool temperature and a mid-infrared powerlaw component consistent with lower-redshift galaxies ($\alpha_{\text{MIR}} \approx 2$) can rectify the perceived global offset from the expected IRX- β relationship.

4. OUTLOOK FOR FUTURE ALMA DATASETS

The current 1.2 mm ALMA deep field datasets have only begun to scratch the surface of possible blank-field ALMA constraints. While perhaps some models and predictions would have expected many more sources in 1.2 mm maps than exist – either as a reflection of the

⁹ Instead of adopting a fixed range of dust temperatures irrespective of IR luminosity, here we adopt the observed $L_{\text{IR}} - \lambda_{\text{peak}}$ relationship shown in C18. The scatter in SEDs is similar to the original assumptions of Capak et al. (2015).

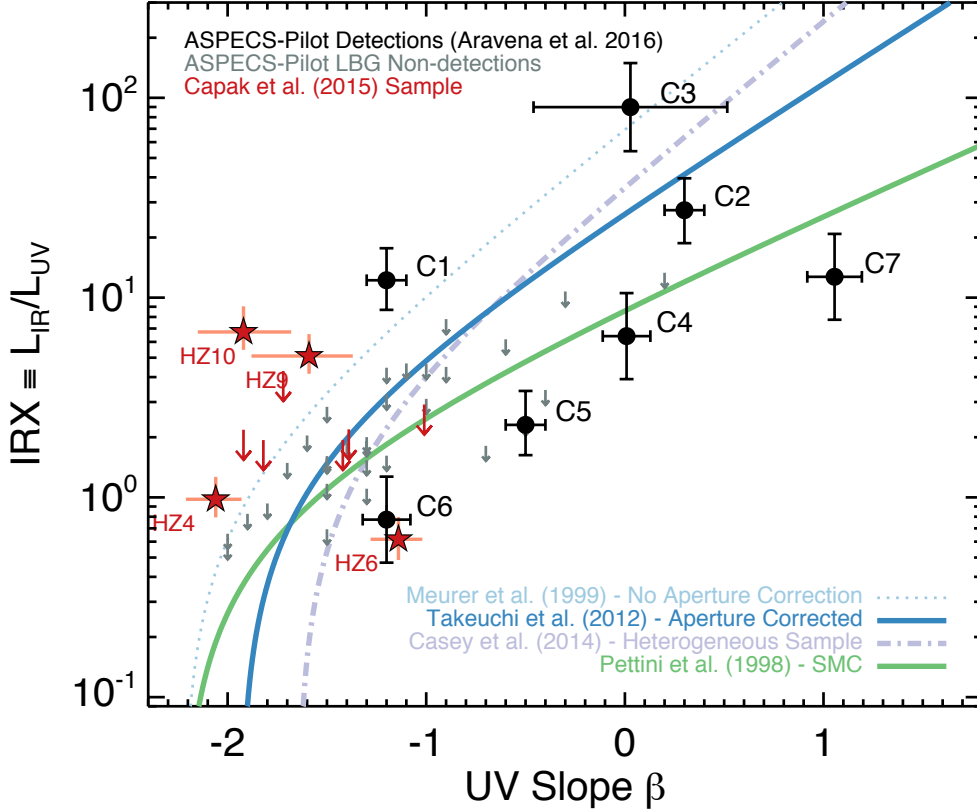


Figure 9. The IRX- β relationship for the LBG galaxies described in B16. The seven detections that have OIR counterparts (Aravena et al. 2016a) are shown as black points. LBGs in the ASPECS-Pilot map without direct detections are shown as gray upper limit arrows. The $z \sim 5.5$ galaxies from Capak et al. (2015) are also shown in red with updated β values from Barisic et al. (2017); those with dust continuum detections are stars, while upper limits are arrows. The scatter of data points here about the Takeuchi et al. (2012) IRX- β relation (thick blue line) for detected sources is representative of intrinsic scatter in galaxy populations based on dust geometry; the fact that more skew below the IRX- β relationship perhaps indicates more consistency with and SMC-type curve (green line). The upper limits given by non-detections cannot rule out either SMC or Milky Way-type dust, which is inconsistent with the findings of B16 that claim high- z sources fall below the SMC curve with 95% confidence. We attribute the difference in conclusions to the adopted form of the far-infrared SED in addition to the difference between the Meurer et al. and Takeuchi et al. curves. We also overplot the Meurer et al. (1999) and Casey et al. (2014b) curves as dotted light blue and dot-dashed lavender, respectively.

steepness of the faint-end of the UV luminosity function, or the potentially dust-rich Universe that might have been – our work suggests that what has been found so far is perfectly consistent with expectation from brighter source, single-dish surveys. This does not mean to imply that the Universe is *less* dusty than previously thought, nor does it mean that there is a measured statistical absence of dusty galaxies where they should have been. In fact, even the most extreme assumptions of the prevalence of DSFGs at high- z , assuming they dominate all of cosmic star-formation at $z > 4$ by over a factor of 10 (i.e. Model B), cannot be ruled out. The fact is that 1.2 mm pencil-beam surveys do not place a good constraint on the relative prevalence of dusty galaxies across a range of redshifts by the very nature of their design.

The reason this uncertainty still plagues our efforts to characterize obscured star-formation in the early Universe is because our community has focused on the design of ALMA deep fields much the way the UV/optical community focused and designed deep fields for the *Hubble Space Telescope*. The HDF, HUDF, and HFF (Williams et al. 1996; Beckwith et al. 2006; Lotz et al. 2017) have been extremely rich legacy datasets purely because the galaxy number density is so high, even out to $z \sim 4 - 5$, with non-negligible samples out to $z \sim 10$. The high number density is due directly to the slope of the faint-end of the UVLF, evolving from $\alpha_{\text{LF}}^{\text{UV}} \approx -1.5$ to -2.5 from $4 < z < 10$ (Finkelstein 2016). The IRLF by contrast has a much shallower faint-end slope, reflecting the fact that galaxies do not become significantly dust-obscured until they are sufficiently massive

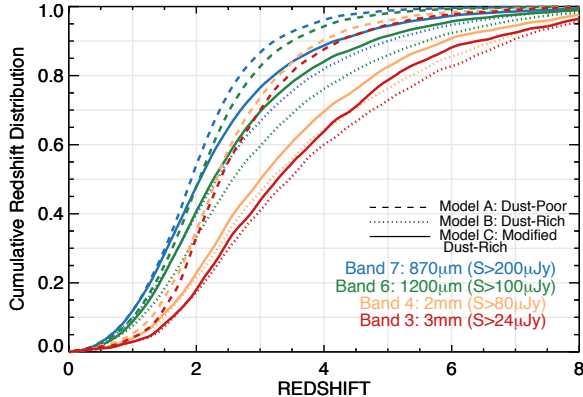


Figure 10. The predicted cumulative redshift distributions for sources identified at $>5\sigma$ in ALMA deep fields conducted at $870\mu\text{m}$ (Band 7; blue), 1.2 mm (Band 6; green), 2.0 mm (Band 4; peach), and 3.0 mm (Band 3; red). The 1σ RMS assumed is for this figure is given in Table 1. Predictions from Model A are shown as a dashed-line, while Model B is dotted and Model C is solid.

(e.g. Whitaker et al. 2017). Independent evidence to the shallowness of this faint-end slope comes from the low number density of dusty systems identified behind clusters, where gravitational lensing can significantly boost sources flux densities (Rawle et al. 2016; González-López et al. 2017). Such a shallow slope, and a relative dearth of very low-mass obscured galaxies, implies that the most fruitful mm-wavelength surveys of galaxies are not the same deep, pencil-beam survey approach that brought us the *Hubble* deep fields.

To evaluate which alternative strategies might be fruitful first requires a re-assessment of the community’s primary science goals. Because ALMA deep fields lack the remarkable source density of the rest-frame UV/optical emission of the *Hubble* (and eventually *JWST*) deep fields, we are unfortunately not able to answer a diverse range of scientific questions with a single data product.

4.1. Needles in the Haystack: Going Deeper does not Reach Farther

The focus of this paper, and C18, is the search for and census of dust-obscured galaxies out to very high-redshifts. What is the intrinsic shape of the IRLF and how do obscured galaxies contribute to the overall star-formation rate density of the Universe? Does the prevalence of DSFGs at high- z provide any useful constraints on the growth of massive galaxies within the first 1-2 Gyr after the Big Bang? Answering these questions in particular requires a systematic follow-up of high- z dust-continuum detected galaxies.

As described in § 2 we extend the C18 model into the ALMA depth, sensitivity and resolution regime by also simulating blank-fields from $870\mu\text{m}$ – 3 mm . Following the same procedure as in § 3, to compare with 1.2 mm existing surveys, we model the redshift distributions for $870\mu\text{m}$ (band 7), 1.2 mm (band 6), 2 mm (band 4) and 3 mm (band 3) for each of the three models (A, B, and C) in Figure 10. The optimum best-fit values of α_{LF} are used for Models A and B (-0.69 and -0.49 , respectively), and the depths given represent the conservative 5σ cut as was deemed necessary in § 3 to avoid high rates of false positives. Overall, Model A (the dust-poor model) skews towards lower redshifts, Model C is at higher redshifts, and Model B skews towards slightly higher redshifts yet. Following the pattern seen for brighter sources in C18, shorter wavelength surveys selects sources at lower redshifts. The median redshifts for Band 7 selected sources is $1.9 < \langle z_{870} \rangle < 2.5$, while Band 6 ranges from $2.0 < \langle z_{1.2\text{mm}} \rangle < 2.7$, Band 4 spans $2.3 < \langle z_{2\text{mm}} \rangle < 3.2$, and Band 3 spans $2.4 < \langle z_{3\text{mm}} \rangle < 3.6$.

A natural question that follows is whether pushing these surveys deeper would result in more high-redshift detections, across any or all of these bands. For example, the ASPECS project has pushed the depth of the HUDF map to ASPECS-Pilot depth across the full 4.5 arcmin^2 . Our model predicts between 60–70 sources detected above $>5\sigma$ significance (with $12\mu\text{Jy/beam}$ RMS at 1.2 mm), a median redshift between $\langle z \rangle = 2.0 - 2.6$ and between 2–9 sources at $z > 4$. Similarly deep $870\mu\text{m}$ surveys (where $\text{RMS}_{870} \approx 2 \times \text{RMS}_{1.2}$) produce nearly identical samples, though even fewer detections at $z > 4$ due to the slightly less advantageous negative K-correction. While it is true that the larger statistical samples that will come with such surveys will be a great help in characterizing higher redshift obscured galaxies, the $z > 4$ sources will truly be needles in the haystack: their spectroscopic identification will likely be exceedingly difficult, and it will not be immediately clear which sources are at $z > 4$ as opposed to $2 < z < 4$.

Pushing even deeper, to $\sim\mu\text{Jy}$ flux densities, what might we expect to find? At these depths, it is still true that only a minority of sources, $\sim 5\text{--}20\%$ no matter the adopted model, will sit at the highest redshifts. In a 1 arcmin^2 survey at 1.2 mm to $1\mu\text{Jy}$ RMS, our model A suggests detection of ~ 130 sources, 9 of which would sit at $z > 4$. Model B suggests detection of ~ 190 sources, 40 of which would sit at $z > 4$. The modeled flux densities of the highest-redshift sources span the whole range, $5\mu\text{Jy}$ up to $\sim 2\text{ mJy}$, similar to the low redshift sources in the mock map. Though this μJy regime is potentially fruitful and insightful to dust emis-

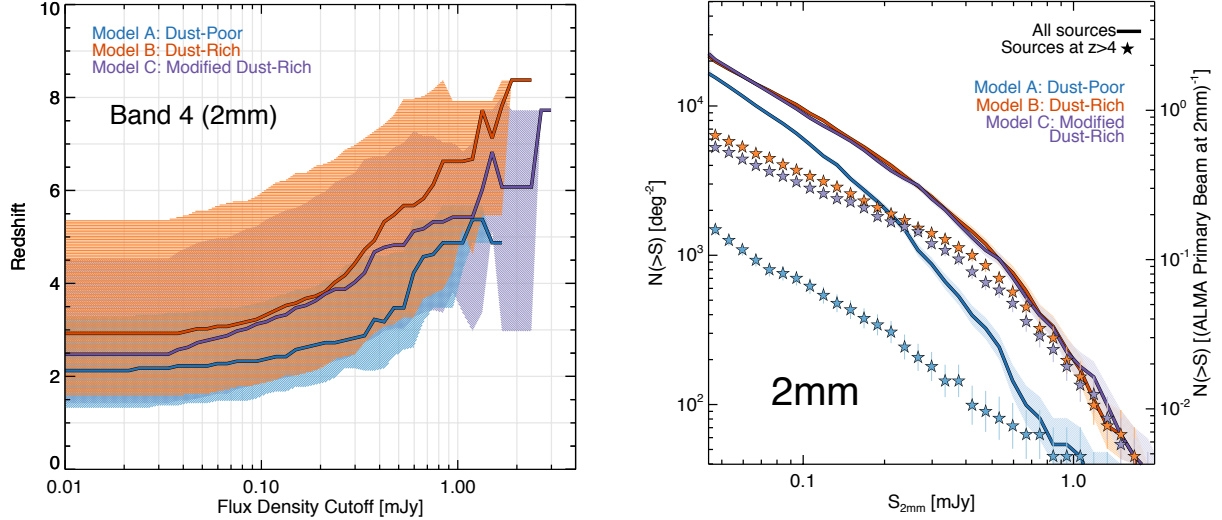


Figure 11. Left: The median redshift of our different models (A, B, and C) as a function of cutoff flux density at 2 mm. The shaded region enclosed in the inner 68% of the samples. This figure shows that constraining 2 mm redshift distributions would be able to distinguish between, e.g. model A (dust-poor) and B and C (dust-rich) with modest sample sizes, 20–100 galaxies. The flux density regime most sensitive to high-redshifts is 0.2–1.0 mJy. Right: the expected number counts at 2 mm in our three different models (solid lines). For each model, we give the number counts of sources above $z > 4$ (stars). Note that models B & C predict that nearly *all* of the 2 mm number counts above 0.5–0.6 mJy should lie at $z > 4$.

sion mechanisms across a range of redshifts, the time investment required to map such areas is prohibitively large by today’s standards: requiring almost two weeks of on-source time for a single 1.2 mm, 0.1 arcmin² pointing. Furthermore, additional precautions are necessary for such observations given the anticipated dynamic range of sources that are likely to exceed the standard factor of ~ 100 between the brightest source in the map and the very deep target RMS.

Taking a step back and returning to Figure 10, it is clear that some surveys are going to be more efficient avenues for characterizing high-redshift sources than others. In particular, surveys in Band 4 and Band 3 would provide much higher redshift samples by effectively filtering out low redshift interlopers. This filtering will greatly simplify the process of identifying and characterizing the highest redshift sources, as a much larger fraction of the identified samples will sit at $z > 4$ (jumping from 2–10% at ~ 1 mm to 30–60% at 2 mm or 3 mm, depending on depth). Whether or not a survey is conducted at 2 mm or 3 mm depends very much on the studies’ more precise goals.

4.2. A Case for 2 mm ALMA Surveys

In C18, we advocate for 2 mm single-dish surveys as an ideal tool for taking census of dust-obscured galaxies beyond $z \sim 4$. Indeed, that regime is the most sensitive to extremely luminous (and rare) starbursts that might have formed the first massive galaxies less than 1 Gyr af-

ter the Big Bang. In this paper, we shift focus to slightly fainter flux densities, smaller area surveys achievable by ALMA. Figure 11 shows the anticipated average redshift of a 2 mm-selected sample as a function of flux density cutoff, and also the number density of sources expected for each model as a function of flux density. Mirroring the predictions of Figure 12 in C18, here we see that brighter 2 mm sources are those that are expected to sit at the highest redshifts. Given this prediction, is there any value in pursuing 2 mm surveys with ALMA instead of single-dish facilities like the IRAM 30 m, JCMT, or the LMT?

We conclude that there is significant value in an ALMA mapping of the sky in Band 4 for a few reasons. Currently, there is no immediate plan to carry out a large-field 2 mm survey with a single-dish facility to ~ 0.1 mJy sensitivity. Given the imminent launch of the *James Webb Space Telescope (JWST)* and its goal of studying galaxy formation and evolution towards very high redshifts, it would be wise for the broad community to have such a 2 mm map in hand as soon as possible to maximize 2 mm source *JWST* follow-up strategy.

A second reason such a blind-field band 4 mapping would be valuable is due to the ease with which multiwavelength counterpart identification and characterization can be carried out, in contrast to the difficult work of counterpart identification for large beamsizes of single-dish work. It is particularly true for high-redshift DSFGs that it will be challenging to identify multiwave-

length characteristics because they will lack the radio or bright mid-infrared counterparts often used for cross-band matching (Roseboom et al. 2010, 2012; Magdis et al. 2011; Casey et al. 2012b,a) due to the contrasting K -corrections between those wavelength regimes (where it is positive) and the millimeter (where it is very negative). A top priority of any such survey will be swift source follow-up to determine redshifts; knowing the sources' position precisely allows for a diverse range of multiwavelength follow-up, from the optical and near-infrared through radio. While single-dish 2 mm maps will cover substantially more area (though requiring significant time allocations on such single-dish facilities), it is probable that redshift confirmation will need to rely on facilities like ALMA for detection of CO or CII, and that fewer options for follow-up will be a result of lack of precision on sources' positions.

Though single-dish 2 mm surveys will always be able to cover much larger areas of the sky than ALMA, we find that a Band 4 map with $\sim 1\text{--}2''$ beam-size, 0.08 mJy/beam RMS, and an area $\sim 230 \text{ arcmin}^2$ matched to the area coverage of deep OIR surveys like CANDELS would result in 20 (Model A) to 120 detections (Models B & C), providing sufficient statistics to distinguish between these broad models, or favor a new model somewhere between these extremes. Such a survey is possible with 50 hours investment in ALMA time, and in band 4, would not risk resolving out emission on spatial scales $< 1''$; although this time investment is significant, it would be possible to carry out during non-optimal weather conditions on the Chajnantor Plateau and therefore would be fairly easy to complete.

4.3. 3 mm Dust Continuum as a Unique Tool

Nominally, ALMA Band 3 (3 mm) would not be an efficient band to search for dust continuum emitters because galaxies' dust emission is significantly fainter at 3 mm than at 2 mm due to the flux density fall off on the Rayleigh-Jeans side of the cold dust blackbody. Indeed, galaxies at $z \sim 2$ have an average flux ratio of $S_{3\text{mm}}/S_{2\text{mm}} = 0.22 \pm 0.02$ and galaxies at $z \sim 5$ have $S_{3\text{mm}}/S_{2\text{mm}} = 0.28 \pm 0.04$. The contrast with 1.2 mm flux densities is even more extreme, with $S_{3\text{mm}}/S_{1.2\text{mm}} = 0.04 \pm 0.02$ and $S_{3\text{mm}}/S_{1.2\text{mm}} = 0.09 \pm 0.03$ at $z \sim 2$ and $z \sim 5$, respectively. Given such low flux densities at 3 mm, and the fact that 3 mm continuum will be more impacted by CMB heating than shorter wavelengths, observations must be significantly more sensitive than surveys at 2 mm.

However, the lion's share of ALMA Band 3 extragalactic observations target low-J transitions of CO to study intermediate redshift galaxies' molecular gas content.

CO(2-1) is accessible in Band 3 at $1.0 < z < 1.7$, while CO(3-2) is accessible in Band 3 from $2.0 < z < 3.1$. Because such observations require deep sensitivity across frequency channels $\sim 10 \text{ MHz}$ wide (with the goal of detecting an emission feature peaking at a few mJy across a few hundred km/s), they are extraordinarily sensitive in continuum across the 8 GHz total bandwidth. Aravena et al. (2016a) highlight the depth of 3 mm continuum observations in the ASPECS-Pilot project, achieving a continuum RMS of $3.8 \mu\text{Jy/beam}$. This depth was achieved primarily to detect transitions of low-J CO blindly (Walter et al. 2016; Decarli et al. 2016a,b), but it is also sufficiently deep to detect dust continuum¹⁰. Aravena et al. (2016a) present one source, C1 (at $z = 2.543$), that is detected in their 0.79 arcmin^2 Band 3 pointing. What more might we expect to see in 3 mm dust continuum maps?

Figure 12 shows what our three models predict for the median redshift of and number counts of 3 mm continuum-detected sources, following the format of Figure 11. Though 3 mm flux densities for matched sources are $\sim 1/5$ of the flux densities at 2 mm, the redshifts are slightly higher (given the extreme negative K -correction at 3 mm, which is even more steep than 2 mm). Like 2 mm, 3 mm mapping has the potential for distinguishing between extreme models like Model A and Model B. At the depth of the ASPECS-Pilot project ($S > 0.02 \text{ mJy}$), Model A predicts one source per ALMA primary beam, while Models B and C predict three (in both cases they are thought to sit at $z < 4$ more likely than at higher redshifts given the depth). Both are statistically consistent with the measured one source found.

Though 3 mm mapping is prohibitive for the purposes of finding and detecting dust continuum emitters, its dual purpose of following-up lower redshift sources in molecular gas observations render Band 3 observations as a unique tool for constraining the high-redshift IRLF, as much of the data have already been taken. For example, with ~ 100 Band 3 pointings at 3 mm (covering an effective area of $\sim 90 \text{ arcmin}^2$) we can begin to constrain the 3 mm number counts and hone in on constraints for the IRLF (J. Zavala et. al., in preparation).

5. CONCLUSIONS

This paper has extended the backward evolution model from Casey et al. (2018) into the regime of ALMA, allowing deeper and higher resolution obser-

¹⁰ Note that flat-spectrum radio sources can also generate emission at 3 mm, although such sources are much more rare by number than dusty galaxies. For example, scaling from the 4.8 GHz number counts of Tucci et al. (2011), we estimate a source density of 10^{-7} deg^{-2} for such synchrotron sources.

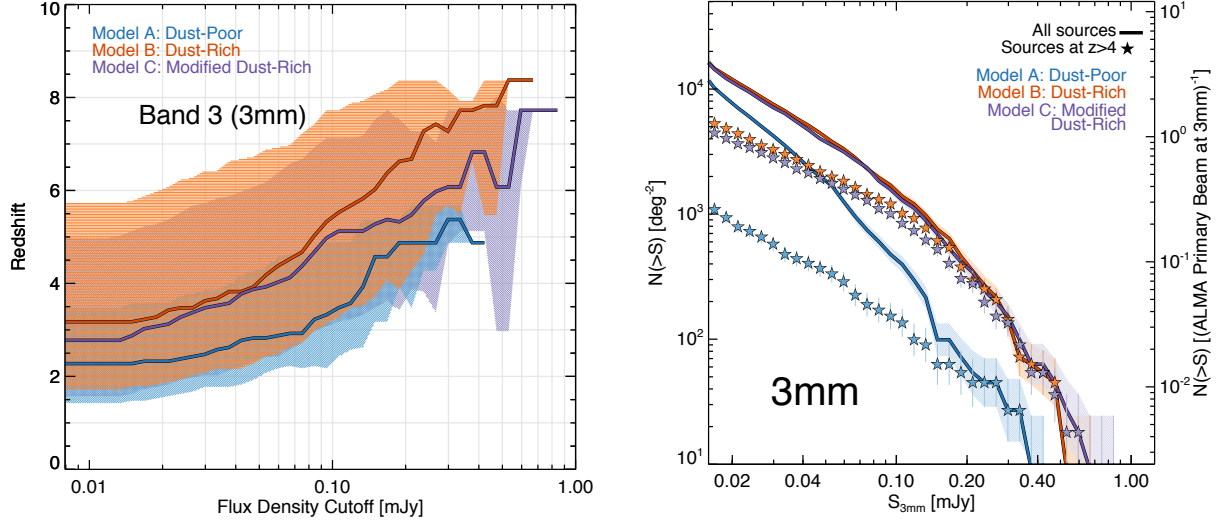


Figure 12. This figure is identical to Figure 11 but provides the median redshift and cumulative number counts for 3 mm surveys.

variations than single-dish facilities. The purpose of our analysis has been to synthesize existing measurements of 1.1–1.3 mm ALMA deep fields with submm/mm single-dish surveys, which generally detect more intrinsically luminous DSFGs. A simple extension of the C18 models appears to reproduce the 1.2 mm ALMA number counts well, although measurement errors for data samples are quite large. We use the source density of Dunlop et al. (2016) to refine our model estimates of the faint-end slope of the IRLF at $z \lesssim 2.5$, and devise a third model which is a variant on the dust-rich model, Model C, where the faint-end slope, α_{LF} , evolves to become shallower with increasing redshift. With larger 1.2 mm surveys combined with the progress of single-dish surveys, we may soon be able to refine the measurement of the faint-end slope of the IRLF out to $z \sim 3$.

We find 1.2 mm ALMA deep fields completely unconstraining for the high-redshift IRLF. Because the faint-end slope of the IRLF is much shallower than the UVLF, deeper observations do not imply that we will detect higher-redshift samples closer to the detection limit. In fact, we find quite the opposite. The brightest sources at 1.2 mm, 2 mm and 3 mm are expected to sit at much higher redshifts than their faintest sources. Finding the highest redshift galaxies requires wider, shallower surveys.

We examine the measured redshift distributions from 1.2 mm deep fields: including the ASPECS-Pilot survey covering 0.79 arcmin² (Aravena et al. 2016a), the HUDF ALMA Deep Field covering 4.4 arcmin² (Dunlop et al. 2016), and the GOODS-ALMA Deep Field covering 69 arcmin² (Franco et al. 2018). The limited statistics of these surveys (limited to 5, 5, and 15 sources

detected above 5σ , respectively) do not allow us to draw conclusions as to which of our three models fits the data best. The largest dataset from Franco et al. (2018) is significantly limited by their resulting delivered spatial resolution ($\sim 0.2''$ beam), which likely led to severe sample incompleteness for resolved sources (most DSFGs are expected to have millimeter sizes $\sim 0.4\text{--}0.5''$ in FWHM; Hodge et al. 2016).

We also explore measurements of the dust content of UV-selected galaxies and contrast with the analysis of Bouwens et al. (2016) and Capak et al. (2015). Both works have claimed that UV-selected populations appear to be significantly less dusty than expected given their rest-frame UV colors and/or stellar masses. We reassess some of the base assumptions made in this claim, primarily with the assumed IR SEDs, and conclude that there is no evidence for less dust in high- z UV-selected galaxy populations. Unlike other works in the literature that claim the UV-selected galaxies require much hotter dust temperatures to fall in-line with the local IRX- β relationships, we find that such hot temperatures are not required to find consistency from low- z to high- z . We caution that future conclusions on the dust content of high- z galaxies require a more thorough analysis of galaxies' IR SEDs, and should ideally not be limited to a single photometric point. Similarly, simplistic assumptions about high- z galaxy SEDs should be replaced with a more rigorous analysis of SEDs across galaxy populations and environments.

With the goal of pushing our understanding of dusty galaxies toward the Epoch of Reionization in mind, then a much more optimal strategy for ALMA would be to map out somewhat wider and shallower 2 mm surveys.

The 2 mm wavelength regime benefits significantly from the very negative K -correction (see Casey, Narayanan, & Cooray 2014a, Figure 3), in such a way that filters out lower redshift $z \sim 1 - 3$ sources that have already been well-characterized in terms of their volume density and bulk contribution to cosmic star-formation. We suggest that an ALMA Band 4 survey of order $\sim 230 \text{ arcmin}^2$ to an RMS of $\sim 0.08 \text{ mJy}$ and a beamsize $\sim 1\text{--}2''$ will have between 20–120 galaxy detections, a median redshift between $3 < z < 4.5$, and a long tail out to very high- z . This dataset would easily distinguish between competing models for the early Universe IRLF. Inference of the IRLF at these epochs will have direct implications for the prevalence of dusty starbursts during the EoR at $z > 6$. We have also analyzed the potential of the 3 mm band to detect dust continuum sources; though observations require much more depth, as galaxies’ 3 mm flux densities will be intrinsically much lower than at 2 mm. However, this depth is routinely achieved in observations intended for molecular line analysis (often the detection of low- J transitions of CO in moderate redshift galaxies). An analysis of the 3 mm number counts already available in the ALMA archive will follow in Zavala et. al., in preparation.

This paper has shown that the optimum design of ALMA deep fields is not necessarily obvious, is highly dependent on the driving science goal, and does not follow the same logic as was used to motivate the legacy deep field products of the *Hubble Space Telescope*, and soon, the *James Webb Space Telescope*. It is the combination of the strong negative K -correction in the sub-millimeter/millimeter and the shallow faint-end slope of the IRLF in comparison to the UVLF (likely caused by the correlation of obscuration with galaxy stellar mass) that drive the observed differences between *HST* deep fields and ALMA deep fields. We find that the search for high-redshift dusty galaxies would be optimized at 2 mm using somewhat wider, and shallower survey mapping strategies. ALMA can contribute significantly to our constraints on dust in the first few billion years of the Universe’s history through targeted 2 mm surveys and large scale analysis and expansion of 3 mm dual-purpose archival datasets.

The authors wish to thank the Aspen Center for Physics for hosting two summer workshops, “The Obscured Universe: Dust and Gas in Distant Starburst Galaxies” in summer 2013 and “New Frontiers in Far-infrared and Sub-millimeter Astronomy” in summer 2016, whose stimulating conversations led to this work. The Aspen Center for Physics is supported by National Science Foundation grant PHY-1066293. CMC thanks the National Science Foundation for support through grant AST-1714528, and additionally CMC and JAZ thank the University of Texas at Austin College of Natural Sciences for support. JS thanks the McDonald Observatory at the University of Texas at Austin for support through a Smith Fellowship. EdC gratefully acknowledges the Australian Research Council for funding support as the recipient of a Future Fellowship (FT150100079). JAH acknowledges support of the VIDI research programme with project number 639.042.611, which is (partly) financed by the Netherlands Organisation for Scientific Research (NWO). SLF acknowledges support from an NSF AAG award AST-1518183. This paper makes use of the following ALMA data: 2012.1.00173.S, 2012.1.00756.S, 2013.1.00718.S, 2013.1.00162.S, 2015.1.00543.S, and 2017.1.00755.S. ALMA is a partnership of ESO (representing its member states), NSF (USA) and NINS (Japan), together with NRC (Canada), MOST and ASIAA (Taiwan), and KASI (Republic of Korea), in cooperation with the Republic of Chile. The Joint ALMA Observatory is operated by ESO, AUI/NRAO and NAOJ.

Many of the datasets this paper and analyses have only been made possible by those that were obtained on the summit of Maunakea on the island of Hawai’i. The authors wish to recognize and acknowledge the very significant cultural role and reverence that the summit of Maunakea has always had within the indigenous Hawaiian community. Astronomers are most fortunate to have the opportunity to conduct observations from this mountain.

REFERENCES

- ALMA Partnership, Vlahakis, C., Hunter, T. R., et al. 2015, ApJL, 808, L4
- Ando, R., Nakanishi, K., Kohno, K., et al. 2017, ApJ, 849, 81
- Andrews, S. M., Wilner, D. J., Zhu, Z., et al. 2016, ApJL, 820, L40
- Aravena, M., Decarli, R., Walter, F., et al. 2016a, ArXiv e-prints, arXiv:1607.06769
- . 2016b, ArXiv e-prints, arXiv:1607.06772
- Barger, A. J., Cowie, L. L., Sanders, D. B., et al. 1998, Nature, 394, 248

- Barisic, I., Faisst, A. L., Capak, P. L., et al. 2017, *ApJ*, 845, 41
- Beckwith, S. V. W., Stiavelli, M., Koekemoer, A. M., et al. 2006, *AJ*, 132, 1729
- Behrens, C., Pallottini, A., Ferrara, A., Gallerani, S., & Vallini, L. 2018, *ArXiv e-prints*, arXiv:1802.07772
- Bothwell, M. S., Aguirre, J. E., Chapman, S. C., et al. 2013, *ApJ*, 779, 67
- Bouwens, R. J., Illingworth, G. D., Franx, M., & Ford, H. 2007, *ApJ*, 670, 928
- Bouwens, R. J., Illingworth, G. D., Oesch, P. A., et al. 2015, *ApJ*, 803, 34
- Bouwens, R. J., Aravena, M., Decarli, R., et al. 2016, *ApJ*, 833, 72
- Brisbin, D., Miettinen, O., Aravena, M., et al. 2017, *ArXiv e-prints*, arXiv:1708.05748
- Buat, V., Iglesias-Páramo, J., Seibert, M., et al. 2005, *ApJL*, 619, L51
- Burgarella, D., Buat, V., & Iglesias-Páramo, J. 2005, *MNRAS*, 360, 1413
- Capak, P. L., Carilli, C., Jones, G., et al. 2015, *ArXiv e-prints*, arXiv:1503.07596
- Carniani, S., Maiolino, R., De Zotti, G., et al. 2015, *A&A*, 584, A78
- Casey, C. M. 2012, *MNRAS*, 425, 3094
- Casey, C. M., Chapman, S. C., Smail, I., et al. 2011, *MNRAS*, 411, 2739
- Casey, C. M., Narayanan, D., & Cooray, A. 2014a, *PhR*, 541, 45
- Casey, C. M., Scoville, N. Z., et al. 2014b, *ApJ*, 796, 95
- Casey, C. M., Berta, S., Béthermin, M., et al. 2012a, *ApJ*, 761, 139
- . 2012b, *ApJ*, 761, 140
- Casey, C. M., Zavala, J. A., Spilker, J., et al. 2018, *ArXiv e-prints*, arXiv:1805.10301
- Chapman, S. C., Blain, A. W., Smail, I., & Ivison, R. J. 2005, *ApJ*, 622, 772
- da Cunha, E., Groves, B., Walter, F., et al. 2013, *ApJ*, 766, 13
- Decarli, R., Walter, F., Carilli, C., et al. 2014, *ApJ*, 782, 78
- Decarli, R., Walter, F., Aravena, M., et al. 2016a, *ArXiv e-prints*, arXiv:1607.06770
- . 2016b, *ArXiv e-prints*, arXiv:1607.06771
- Duncan, K., & Conselice, C. J. 2015, *MNRAS*, 451, 2030
- Dunlop, J. S., McLure, R. J., Biggs, A. D., et al. 2016, *ArXiv e-prints*, arXiv:1606.00227
- Faisst, A. L., Capak, P. L., Yan, L., et al. 2017, *ArXiv e-prints*, arXiv:1708.07842
- Finkelstein, S. L. 2016, *PASA*, 33, e037
- Finkelstein, S. L., Ryan, Jr., R. E., Papovich, C., et al. 2015, *ApJ*, 810, 71
- Franco, M., Elbaz, D., Béthermin, M., et al. 2018, *ArXiv e-prints*, arXiv:1803.00157
- Fujimoto, S., Ouchi, M., Ono, Y., et al. 2016, *ApJS*, 222, 1
- Goldader, J. D., Meurer, G., Heckman, T. M., et al. 2002, *ApJ*, 568, 651
- González-López, J., Bauer, F. E., Romero-Cañizales, C., et al. 2017, *A&A*, 597, A41
- Grazian, A., Fontana, A., Santini, P., et al. 2015, *A&A*, 575, A96
- Gruppioni, C., et al. 2013, *MNRAS*, 432, 23
- Hatsukade, B., Kohno, K., Umehata, H., et al. 2016, *PASJ*, 68, 36
- Hezaveh, Y., Dalal, N., Holder, G., et al. 2016a, *JCAP*, 11, 048
- Hezaveh, Y. D., Marrone, D. P., Fassnacht, C. D., et al. 2013, *ApJ*, 767, 132
- Hezaveh, Y. D., Dalal, N., Marrone, D. P., et al. 2016b, *ApJ*, 823, 37
- Hodge, J. A., Karim, A., Smail, I., et al. 2013, *ApJ*, 768, 91
- Hodge, J. A., Swinbank, A. M., Simpson, J. M., et al. 2016, *ApJ*, 833, 103
- Howell, J. H., Armus, L., Mazzarella, J. M., et al. 2010, *ApJ*, 715, 572
- Hughes, D. H., Serjeant, S., Dunlop, J., et al. 1998, *Nature*, 394, 241
- Laporte, N., Ellis, R. S., Boone, F., et al. 2017, *ApJL*, 837, L21
- Le Flocc'h, E., Papovich, C., Dole, H., et al. 2005, *ApJ*, 632, 169
- Leroy, A. K., Bolatto, A. D., Ostriker, E. C., et al. 2015, *ApJ*, 801, 25
- Lotz, J. M., Koekemoer, A., Coe, D., et al. 2017, *ApJ*, 837, 97
- Madau, P., & Dickinson, M. 2014, *ARA&A*, 52, 415
- Magdis, G. E., Elbaz, D., Dickinson, M., et al. 2011, *A&A*, 534, A15
- Magnelli, B., Popesso, P., Berta, S., et al. 2013, *A&A*, 553, A132
- Marrone, D. P., Spilker, J. S., Hayward, C. C., et al. 2017, *ArXiv e-prints*, arXiv:1712.03020
- McLure, R. J., Dunlop, J. S., Bowler, R. A. A., et al. 2013, *MNRAS*, 432, 2696
- Meier, D. S., Walter, F., Bolatto, A. D., et al. 2015, *ApJ*, 801, 63
- Meurer, G. R., Heckman, T. M., & Calzetti, D. 1999, *ApJ*, 521, 64
- Neri, R., Genzel, R., Ivison, R. J., et al. 2003, *ApJL*, 597, L113

- Ono, Y., Ouchi, M., Kurono, Y., & Momose, R. 2014, *ApJ*, 795, 5
- Oteo, I., Zwaan, M. A., Ivison, R. J., Smail, I., & Biggs, A. D. 2016, *ApJ*, 822, 36
- Pannella, M., Carilli, C. L., Daddi, E., et al. 2009, *ApJL*, 698, L116
- Pannella, M., Elbaz, D., Daddi, E., et al. 2015, *ApJ*, 807, 141
- Pettini, M., Kellogg, M., Steidel, C. C., et al. 1998, *ApJ*, 508, 539
- Planck Collaboration, Ade, P. A. R., Aghanim, N., et al. 2016, *A&A*, 594, A13
- Rafelski, M., Teplitz, H. I., Gardner, J. P., et al. 2015, *AJ*, 150, 31
- Rawle, T. D., Altieri, B., Egami, E., et al. 2016, *MNRAS*, 459, 1626
- Reddy, N. A., & Steidel, C. C. 2009, *ApJ*, 692, 778
- Roseboom, I. G., Oliver, S. J., Kunz, M., et al. 2010, *MNRAS*, 409, 48
- Roseboom, I. G., Ivison, R. J., Greve, T. R., et al. 2012, *MNRAS*, 419, 2758
- Sanders, D. B., Mazzarella, J. M., Kim, D.-C., Surace, J. A., & Soifer, B. T. 2003, *AJ*, 126, 1607
- Scoville, N., Aussel, H., Sheth, K., et al. 2014, *ApJ*, 783, 84
- Scoville, N., Sheth, K., Aussel, H., et al. 2016, *ApJ*, 820, 83
- Scoville, N., Lee, N., Vanden Bout, P., et al. 2017, *ApJ*, 837, 150
- Smail, I., Ivison, R. J., & Blain, A. W. 1997, *ApJL*, 490, L5+
- Song, M., Finkelstein, S. L., Ashby, M. L. N., et al. 2016, *ApJ*, 825, 5
- Strandet, M. L., Weiss, A., De Breuck, C., et al. 2017, *ApJL*, 842, L15
- Tacconi, L. J., Neri, R., Chapman, S. C., et al. 2006, *ApJ*, 640, 228
- Tacconi, L. J., et al. 2008, *ApJ*, 680, 246
- Takeuchi, T. T., Buat, V., Heinis, S., et al. 2010, *A&A*, 514, A4
- Takeuchi, T. T., Yuan, F.-T., Ikeyama, A., Murata, K. L., & Inoue, A. K. 2012, *ApJ*, 755, 144
- Tucci, M., Toffolatti, L., de Zotti, G., & Martínez-González, E. 2011, *A&A*, 533, A57
- Umehata, H., Tamura, Y., Kohno, K., et al. 2015, *ApJL*, 815, L8
- van der Wel, A., Franx, M., van Dokkum, P. G., et al. 2014, *ApJ*, 788, 28
- Vieira, J. D., Marrone, D. P., Chapman, S. C., et al. 2013, *Nature*, 495, 344
- Walter, F., et al. 2016, *ApJ*
- Wardlow, J. L., Smail, I., Coppin, K. E. K., et al. 2011, *MNRAS*, 415, 1479
- Whitaker, K. E., Pope, A., Cybulski, R., et al. 2017, *ArXiv e-prints*, arXiv:1710.06872
- Whitaker, K. E., Franx, M., Leja, J., et al. 2014, *ApJ*, 795, 104
- Williams, R. E., Blacker, B., Dickinson, M., et al. 1996, *AJ*, 112, 1335